

Multi-Vortex Distributor: Effect on 2-D Fluidized Bed Reactor Performance

by

HG Brink

A dissertation submitted in partial fulfilment of the requirements for the degree

Master of Engineering (Chemical Engineering)

in the

Department of Chemical Engineering

***Faculty of Engineering, the Built Environment and Infor-
mation Technology***

University of Pretoria

21 June 2011

Multi-Vortex Distributor: Effect on 2-D Fluidized Bed Reactor Performance

Author : H G Brink
Supervisor : W Nicol
Department : Chemical Engineering, University of Pretoria
Degree : Master of Engineering (Chemical Engineering)

Synopsis

The influence of the distributor configuration on the mass transfer and bubble sizes in a 2-D FBR was studied for two types of distributor configurations:

- A novel multi-vortex (MV) distributor with tuyères directed vertically and horizontally at different heights.
- A standard perforated plate distributor (baseline).

The ozone decomposition reaction over FCC catalyst was used as an indirect measure of the interphase mass transfer in the bed. The U_0 ranged between 0.1 m/s and 0.35 m/s, with air as a fluidizing medium at ambient conditions.

The MV distributor displayed a significant improvement in the conversion $\left(\frac{x_{measured}}{x_{PFR}}\right)$. For all velocities an improvement of between 0% and 30% was measured (average improvement of 14.7%). At $U_0 \geq 0.2$ m/s the improvement distributed evenly about the mean improvement, with a minimum improvement of 10%.

The U_c for the respective distributors were determined using absolute pressure fluctuations (baseline distributor) and visual observations (MV distributor) and it was found that the U_c for the MV distributor was lower than that for the baseline:

- $U_{c\ Baseline} = 0.30$ m/s
- $U_{c\ MV\ distributor} = 0.25$ m/s

The decrease in U_c indicated that the MV distributor induces faster onset of turbulent behaviour in the FBR which negates interphase mass transfer limitations in the FBR.

The bubble sizes were measured visually and compared to a pressure signal decomposition technique. The bubble size growth for the MV distributor was estimated at 1.4 times that of the baseline.

Two models were compared to the experimental results, the Kunii-Levenspiel three-phase model and the Thompson generalized bubble-turbulent model. The fitting parameters showed that the mass transfer for the MV distributor is significantly larger than that of the baseline. In addition the MV distributor decreased the axial dispersion in the FBR as $U_0 \rightarrow U_\infty$, which improved the reactor performance to that of an ideal PFR. This phenomenon was observed at $U_0 > 0.33 \text{ m/s}$.

KEYWORDS: Kunii-Levenspiel model, Thompson model, pressure fluctuation analysis

Table of Contents

Synopsis.....	i
Nomenclature.....	iii
1 Introduction	1-1
2 Literature.....	2-1
2.1 Background.....	2-1
2.2 Distributor Design Influence on FBR Hydrodynamics	2-3
2.2.1 Distributor design (Kunii & Levenspiel, 1991:95).....	2-3
2.2.2 Horizontal Injection of Gas	2-4
2.3 Determining the Bubble-Turbulent Regime Transition Boundary (Bi, HT, Ellis & Grace, 2000).....	2-4
2.3.1 Visual observations	2-5
2.3.2 Pressure Fluctuations.....	2-5
2.4 Pressure Fluctuation Relation to Bubble Size (Van der Schaaf et al., 2002)	2-6
2.4.1 Decomposing the Pressure Time Series	2-6
2.4.2 Components of Pressure Fluctuations in a FBR.....	2-7
2.5 Modeling Catalytic Fluidized Bed Reactors.....	2-9
2.5.1 Kunii and Levenspiel Three Phase Model (K-L model) (Levenspiel, 1999: 455).....	2-9
2.5.1.1 The Mathematic Representation of the K-L Model:.....	2-10
2.5.1.1.1 Material Balances:	2-10
2.5.1.1.2 Parameter Estimation	2-11
2.5.1.1.3 Catalytic Reactions:	2-11
2.5.1.2 Model Analysis.....	2-13
2.5.2 Grace Two-Phase Bubbling Model (G2PM) (Grace, 1984)	2-13
2.5.2.1 Mathematical Representation of the G2PM	2-13

2.5.2.1.1	Mole Balances	2-13
2.5.2.1.2	Material Balances	2-15
2.5.2.1.3	Parameter Estimation	2-16
2.5.2.2	G2PM Analysis	2-17
2.5.3	Thompson Model (Thompson <i>et al.</i> , 1999; Abba <i>et al.</i> , 2003).....	2-18
2.5.3.1	Single Phase Axially Dispersed Plug Flow Model (ADPFM)	2-19
2.5.3.2	G2PM and ADPFM Convergence	2-20
2.5.3.3	Implementation of the Thompson Model	2-22
3	Experimental setup	3-1
3.1	Equipment.....	3-1
3.1.1	Fluidized bed Reactor	3-1
3.1.1	Packed Bed Reactor (PBR).....	3-3
3.1.2	Distributors	3-3
3.1.3	Visible Bubble Size Measurements	3-6
3.1.4	Data Acquisition	3-6
3.2	Catalyst Preparation	3-6
3.2.1	Catalyst Activity	3-6
3.3	Method.....	3-10
3.3.1	FBR Ozone Measurements.....	3-10
3.3.2	Visual Bubble Size Analysis	3-10
4	Results and Discussions	4-1
4.1	Ozone Measurements.....	4-1
4.2	Determining the bubbling to turbulent regime transition boundary	4-3
4.3	Bubbles Sizes	4-4
4.3.1	Visual Bubble Size Measurements.....	4-4
4.3.2	Bubble Size Analysis Using Pressure Fluctuations	4-5
4.4	Model Predictions	4-6

4.4.1	Kunii-Levenspiel Model (K-L Model).....	4-6
4.4.2	Thompson Model.....	4-9
5	Conclusions	5-1
6	References.....	6-1
<i>Appendix A</i>	List of Investigations on the Bubble-Emulsion Separation in FBRs ..	A-1
<i>Appendix B</i>	Distributor Types and Respective Advantages and Disadvantages (Kunii & Levenspiel, 1991:95)	B-1
<i>Appendix C</i>	Mechanical Drawing of MV Distributor Design	C-1
<i>Appendix D</i>	Particle Size Distributions for Respective Distributor Experiments..	D-1
<i>Appendix E</i>	Video of Comparative Behaviour seen in Respective Distributor Experiments	E-1

Nomenclature

A_c	Reactor cross sectional area	m^2
$ADPFM$	Single phase axially dispersed plug flow model	
A_I	Total interphase transfer surface area, ($= a_I V_{G,L}$)	m^2
a_I	Interphase mass transfer surface area per unit volume of gas in low density phase	m^{-1}
A_{open}	Open area on distributor	mm^2
A_{or}	Area of single orifice	mm^2
Ar	Archimedes number, ($\equiv \frac{d_p^3 \rho_G (\rho_S - \rho_G) g}{\mu_G^2}$)	
$a_y(t)$	The attenuation of the coherent global pressure fluctuations	
$b_y(t)$	The contribution of the gas bubbles or turbulence to $p_y(t)$	kPa
CFD	Computational fluid dynamics	
C_i	Gas concentration of species i	$kmol/m^3$
$C_{i,IN}$	Inlet concentration of species i	$kmol/m^3$
$C_{i,OUT}$	Outlet concentration of species i	$kmol/m^3$
$COP_{xy}(f)$	The coherent-output PSD	kPa^2/Hz
$CSTR$	Continuously stirred tank reactor	
\mathcal{D}	Gas diffusion coefficient	m^2/s
d_b	Bubble volume-equivalent diameter	m
d_p	Average particle size	m

D_t	Reactor Diameter	m
D_z	Axial dispersion coefficient	m^2/s
FBR	Fluidized bed reactor	
FCC	Fluidized catalytic cracking	
f	The frequency domain of the Fourier analysis used to calculate Φ	Hz
f_b	Volume fraction of solids in bubble to volume of bed	
f_c	Fraction of total solids in cyclones and dipleg during normal operation	
f_{cl}	Volume fraction of solids in cloud to volume of bed	
f_e	Volume fraction of solids in emulsion to volume of bed	
$f_{K_{bc}}$	Coefficient in K_{bc} correlation	
$f_{K_{ce}}$	Coefficient in K_{ce} correlation	
f_{k_q}	Coefficient in k_q correlation	
f_{Pe}	Coefficient in Pe correlation	
$\mathcal{F}_x(f)$	The one-sided Fourier transform of $p_x(t)$	
$\mathcal{F}_x^*(f)$	The complex conjugate of $\mathcal{F}_x(f)$	
g	Gravitational acceleration	$9.81 m/s^2$
G2PM	Grace two-phase model with axial dispersion in both phases	
H	Expanded bed height	m
ID	Inner diameter of orifice	mm
$IOP_{xy}(f)$	The incoherent-output PSD	kPa^2/Hz

K_{bc}	Interphase mass transfer coefficient between the bubble and cloud phase	s^{-1}
K_{ce}	Interphase mass transfer coefficient between the cloud and emulsion phase	s^{-1}
$K - L model$	Kunii-Levenspiel three-phase model	
k_q	Interphase mass transfer rate constant	m/s
k_r'''	Reaction rate constant	$\frac{m_{solid}^3}{m_{bed}^3 s}$
$\overline{k_r''''}$	Average reaction rate constant for experimental run	$\frac{m_{solid}^3}{m_{bed}^3 s}$
M	Mass	kg
m_G	Fraction of gas in each phase	
m_S	Fraction of solid in each phase	
M_{S0}	Total solids inventory in reactor	kg
M_S	Solids in fluidized bed ($= (1 - f_c)M_S$)	kg
MV	Multi-vortex	
n	Order of reaction	
N_{or}	Number of orifices in distributor plate	
PBR	Packed bed reactor	
P_B	Probability of being in the bubbling regime	
pdf	Probability density function	
Pe	Peclet Number ($= \frac{U_0 H}{D_z}$)	
PFR	Plug flow reactor	

PSD	Power spectral density	kPa^2/Hz
P_T	Probability of being in the turbulent regime	
$p_x(t)$	The pressure time series measured at position x in the bed	kPa
$p_y(t)$	The pressure time series measured at position y in the bed	kPa
Q	Volumetric flow rate	m^3/s
q	Volumetric flow rate ratio	
$R(C)$	Overall reaction rate expression	$kmol/kg_s$
Re	Reynolds number $(= \frac{\rho_G U_0 d_p}{\mu_G})$	
$r_j(C)$	Reaction rate expression for the j th reaction	$kmol/kg_s$
Sc	Schmidt number $(= \frac{\mu_G}{\rho_G \mathcal{D}})$	
T	The averaging time interval	s
t	The time domain of the pressure fluctuation series $p_x(t)$ and $p_y(t)$	s
U_0	Superficial gas velocity	m/s
U_0^*	Dimensionless superficial gas velocity $(= \frac{Re_0}{Ar^{\frac{1}{3}}})$	
U_{or}	Orifice linear velocity	m/s
U_∞	The velocity at which turbulent flow is fully developed	m/s
U_b	Average bubble rise velocity	m/s
U_b^*	Average velocity of gas through the bubble phase in the K-L model	m/s
u_{br}	Rise velocity of a single bubble in a bed otherwise at U_{mf}	m/s
U_c	Transition velocity to from bubbling to turbulent regime	m/s

U_c^*	Dimensionless transition velocity to turbulent regime ($= \frac{Re_c}{Ar^{\frac{1}{3}}}$)	
$U_{c,exp,j}^*$	Dimensionless transition velocity to turbulent regime, experimentally determined in experiment j ($= \frac{Re_{c,exp,j}}{Ar^{\frac{1}{3}}}$)	
U_{cl}^*	Average velocity of gas through the cloud phase in the K-L model	
U_e^*	Average velocity of gas through the emulsion phase in the K-L model	m/s
U_k	Velocity at which bed is completely in the turbulent regime	m/s
U_{mf}	Minimum fluidization velocity	m/s
U_{min}^*	Dimensionless minimum velocity below which the probability of turbulent behaviour is zero ($= \frac{Re_{min}}{Ar^{\frac{1}{3}}}$)	
u	Superficial gas velocity in each phase	m/s
V	Reactor bed volume	m^3
v_c^*	Normalized transition velocity from bubbling to turbulent fluidization	
x	Conversion of reagent to product	
x/x_{PFR}	Conversion efficiency of reagent to product relative to an ideal plug flow reactor (PFR)	
z	Vertical coordinate measured from the gas distributor	m

Greek letters

α	Volumetric ratio of wake volume to bubble volume
----------	--

α_D	Diffusional combination term for convergence of G2PM to ADPFM	
$\alpha_{R,i}$	Reaction rate combination term for convergence of G2PM to ADPFM	
β	Fitting parameter in logistic regression function	
γ_{xy}^2	Coherence of the normalized ϕ_{xy}	
Δ	The time delay in the fast pressure waves through the FBR	s
δ	Volumetric fraction of bed represented by bubbles	
ϵ	Gas volume fraction	
θ	Injection angle of gas into FBR	
μ_G	Gas viscosity	Pa.s
ν_{ij}	Stoichiometric coefficient for species i and reaction j	
ρ_G	Gas density	kg/m ³
ρ_S	Solid particle density	kg/m ³
ρ	Bed bulk density	kg/m ³
σ_c^*	Normalized standard deviation of uncertainty in bubble-turbulent transition boundary	
$\sigma_{ozone,in}$	Standard deviation of $C_{ozone,in}$	ppm ²
$\sigma_{ozone,out}$	Standard deviation of $C_{ozone,out}$	ppm ²
σ_x	Standard deviation of x	
$\sigma_{xy,c}$	Standard deviation of the coherent pressure fluctuations	kPa
$\sigma_{xy,i}$	Standard deviation of the incoherent pressure fluctuations	kPa
τ	Residence time in the PBR based on volume of catalyst (V_s/Q)	s

$\Phi_{xx}(f)$	The power spectral density (PSD) of $p_x(t)$	kPa^2/Hz
$\Phi_{yy}(f)$	The PSD of $p_y(t)$	kPa^2/Hz
$\Phi_{xy}(f)$	The cross power spectral density (CPSD) of $p_x(t)$ and $p_y(t)$	kPa^2/Hz
$\Phi_{xy}^*(f)$	The complex conjugate of $\Phi_{xy}(f)$	kPa^2/Hz
ϕ	Solid volume fraction	
ϕ_{L0}	Solid volume fraction in the L-phase at lower limit of Thompson model	
ψ	Phase volume fraction	

Subscripts

b	Bubble
B	Bubbling fluidization regime
cl	Cloud
e	Emulsion
f	Total bed
G	Gas
H	Higher density phase
I	Interface between phases
L	Lower density phase
mf	Minimum fluidization
p	Particle
S	Solid
t	Tower (Reactor)



T Turbulent fluidization regime

1 Introduction

Fluidized bed reactors (FBR) are one of the most commonly used commercial reactors in the processing industry for the contacting of heterogeneous reagents (gas-solid, gas-solid-liquid). Fluidization is used in industries as diverse as mineral processing, coal and biomass gasification, power generation, petroleum refining, pharmaceuticals and a myriad of other solids handling processes (Yang, 2003a). The reasons for the use of FBRs are (Yang, 2003b):

- The ease of solids handling due to the liquid like behaviour in the reactor
- Nearly isothermal operation of the FBRs
- Very good heat transfer characteristics

One of the major disadvantages of FBRs is mass transfer limitations due to the movement of components across the bubble-emulsion interphase boundary, which can severely slow down the overall reaction rate in the FBR. The resistance to interphase mass transfer across the bubble-emulsion boundary could result in the gas partially bypassing the fixed fluidised bed (with internal recycle, i.e. bubbling or turbulent fluidized bed). The gas bypassing occurs either by (Geldart & Cranfield, 1972):

- reducing the amount of gas in contact with the solid catalyst. This mechanism occurs in small particle systems in which the bubble velocity is significantly larger than the interstitial gas velocity flowing in the emulsion phase of the bed. The gas remains in the bubbles and thereby bypasses the catalyst in the bed;
- short-circuiting a part of the bed, which occurs in large particle beds in which the bubbles move more slowly than the gas through the emulsion. Due to the pressure gradient through the bed, the gas enters the bubbles from the base and exits via the roof which causes the gas to bypass sections of the bed through the slow moving bubbles.

Apart from the bubble sizes in the FBR, additional effects such as gas-phase to emulsion lateral dispersion and the mass transfer mechanism can affect the mass transfer in the bed which can influence the performance of the FBR.

Due to its influence on FBR performance, a great deal of research has concentrated on reducing the mass transfer limitations in the FBR (Ouyang, F & Levenspiel, 1986; Van Ommen, Nijenhuis & Coppens, 2009; Wormsbecker, Pugsley & Tanfara, 2007; Rowe, Santoro & Yates, 1978; Yan, Huang & Zhu, 2008; Leung, 1972; Sathiyamoorthy & Rao, 1978; Werther, 1978; Upadhyay, Saxena & Ravetto, 1981; Garncarek *et al.*, 1997; Lombardi, Pagliuso & Goldstein, 1997; Chyang & Lin, YC, 2002; Depypere, Pieters & Dewettinck, 2004; Kleijn van Willigen *et al.*, 2005; Christensen *et al.*, 2008; Chyang, Lieu & Hong, 2008).

The scope of this study was to determine the influence of the distributor configuration on a 2-D fluidized bed reactor (FBR) performance. The influence is quantified by the difference in the conversion efficiencies $\left(\frac{x_{measured}}{x_{PFR}}\right)$, interphase mass transfer, onset of turbulent behaviour in the FBR (U_c) and bubble sizes for the different distributor configurations.

The distributor configurations tested were a perforated plate and a novel multi-vortex (MV) distributor with tuyères (injection conduits) in which the injection of gas was directed vertically and horizontally at different heights. The configurations were chosen to try and increase turbulence at the distributor surface which would in turn increase the interphase mass transfer and phase distribution in the FBR.

The fast ozone decomposition reaction (equation 1-1) was used in conjunction with model predictions using the K-L model and Thompson model. The mass transfer coefficients of the respective distributor configurations were quantified by fitting the mass transfer parameters in the two models.



In addition to the mass transfer measurements, the bubble sizes for the respective distributors were visually determined using a frame-by-frame analysis of video footage taken at different velocities. These visual measurements were compared to the $\sigma_{xy,i}$ of the absolute pressure fluctuations measured at the distributor plate and at a height of 300mm above the distributor (Van der Schaaf *et al.*, 2002). The respective U_c values were determined using the standard deviations of the absolute pressure fluctuations in the bed as well as by visual observation of the bed behaviour.

FCC catalyst, impregnated with Fe_2O_3 , was used as a catalyst for the ozone decomposition reaction. The experiments were done at ambient conditions for flow rates ranging from 0.1 m/s to 0.3 m/s.

2 Literature

2.1 **Background**

Fluidized beds are some of the most commonly used reactors in the chemical processing industry. The main reasons for the frequency of application is the short diffusional distances inside the particles, as well as the good heat transfer due to the near ideal mixing in these reactors.

The gas flow characteristics in a FBR, whether in the bubble or emulsion phases, are considered crucial factors in the performance of FBRs. Due to the critical importance of the gas flow behaviour, some of the most important design parameters for FBRs require detailed knowledge of the gas phase flow (Hulme & Kantzas, 2004).

Fluidized beds can suffer from mass transfer limitations as a result of particle-fluid separation, which causes bubbles to form in the bed and induces bypassing of gas to occur. Increasing the gas flow rate increases the bubble size in the bed and this reduces the mass transfer rate between the bubbles and the solids; this can affect the overall reaction rate (Van Ommen *et al.*, 2009; Rowe *et al.*, 1978; Geldart & Cranfield, 1972; Sobrino *et al.*, 2009; Shen, Johnsson & Leckner, 2004; Köksal & Vural, 1998). Figure 2-1 shows the respective mass transfer steps in the FBR for different scales; the bubble-emulsion (Dense Phase – Dilute Phase) mass transfer is usually considered to be the rate limiting mass transfer step.

In addition, bubble and throughflow in the system have the dominant effect on a freely bubbling system because it dictates:

- Gas and solid distribution
- Bed expansion
- Heat/mass transfer between the gas and solid components
- The conversion capabilities in the system

This is a result of the bubbles and throughflow which increases the hydrodynamic mixing in the system (Köksal & Vural, 1998; Shen *et al.*, 2004)

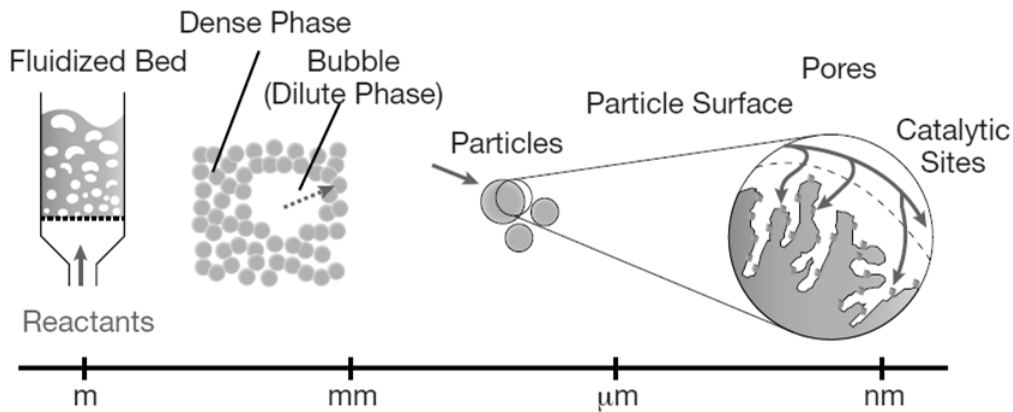


Figure 2-1: The mass transfer of components in the fluidized bed reactor, for different scales. The largest mass transfer limitation is usually experienced between the bubble and emulsion phases (Van Ommen *et al.*, 2009)

Overcoming the bubble-emulsion separation limitation in FBRs have been a subject for investigation for multiple authors (Leung, 1972; Rowe *et al.*, 1978; Werther, 1978; Sathiyamoorthy & Rao, 1978; Upadhyay, Saxena, & Ravetto, 1981; Ouyang, F & Levenspiel, 1986; Sreenivasan & Raghavan, 2002; Garncarek *et al.*, 1997; Lombardi *et al.*, 1997; Chyang & Lin, YC, 2002; Depypere *et al.*, 2004; Kleijn van Willigen *et al.*, 2005; Wormsbecker *et al.*, 2007; Yan *et al.*, 2008; Christensen, Nijenhuis, Van Ommen, & Coppens, 2008; Chyang *et al.*, 2008; Van Ommen *et al.*, 2009). Table A-1 (Appendix A) gives a brief overview of these investigations.

Van Ommen *et al.* (2009) states that the disadvantages of multiphase reactors can be overcome by structuring the beds, thereby decoupling some of the conflicting design objectives in the FBRs. Examples of these conflicting objectives is bubble size vs. high gas flow, conversion vs. turbulence in the bed. Structuring FBRs increases the degrees of freedom in the bed and therefore simplifies the design and scaling of these reactors. Scaling can take place by altering the fluidizing medium or the solid phase of the FBR. In both these cases the change can be either dynamic or geometric. Table 2-1 shows some common procedures of structuring FBRs by these four abovementioned methods (Van Ommen *et al.*, 2009).

Table 2-1: Common possible methods to structure fluidized bed reactors (Van Ommen *et al.*, 2009)

	Dynamics	Geometry
Gas	Pulsation	Distributor
	Vibration	Baffles
	Sound Waves	Staged Injection
	Closed-Loop Control	Membrane Tubes
Particles	Rotation	Particle Size Distribution
	Magnetic Fields	Shape Factor
	Electric Fields	Particle Mixtures

2.2 ***Distributor Design Influence on FBR Hydrodynamics***

The design of the gas distribution system is an important consideration in the design of a FBR (Ouyang, F & Levenspiel, 1986). This is due to the effect the distributor design has on:

- The bubble sizes, paths and numbers which dictate the quality of fluidization and gas bypassing in the system (Ouyang, F & Levenspiel, 1986; Chyang & Lin, YC, 2002).
- The extent of lateral gas dispersion in the FBR (Chyang *et al.*, 2008).
- The heat and mass transfer properties of the FBR (Werther, 1978).
- Inadequate lateral mixing of solids and gas-solid contacting in the FBR (Sreenivasan & Raghavan, 2002).
- The initial distribution of fluidizing gas into the FBR which generates circulation in the solid phase (Garncarek *et al.*, 1997).

2.2.1 Distributor design (Kunii & Levenspiel, 1991:95)

FBR distributor plates can be grouped in five distinct types of distributors, each with its own advantages and disadvantages:

1. Perforated Plates
2. Bubble Caps and Nozzles

3. Spargers
4. Conical Grids
5. Pierced Sheet Grids

The advantages and disadvantages of each of these distributor types are summarized in Table B-1 (Appendix B).

2.2.2 Horizontal Injection of Gas

The gas from conventional FBR distributors (porous plate, perforated plate and multi-vertical nozzle) possesses only axial momentum which causes the gas at any point in the FBR to possess an axial component (vertical component) which significantly exceeds the radial or tangential components (horizontal components). This deficiency in horizontal velocity components reduces the fluid movement and so also the mixing in the FBR (Chyang & Lin, YC, 2002).

Injecting gas into a FBR at an angle θ to the horizontal, the axial component of the gas velocity ($U_0 \sin\theta$) is responsible for the fluidization of the particles in the bed, while the horizontal component ($U_0 \cos\theta$) is responsible for horizontal momentum being transferred to the bed. As the gas enters deeper into the bed a reduction in the horizontal momentum is observed. This reduction can be counteracted by decreasing θ , thereby increasing the mixing of solids in the bed which promotes greater mass transfer in the bed (Sreenivasan & Raghavan, 2002).

The dispersion of gas in the FBR is considered to be a strong function of the distributor type used. Chyang *et al.* (2008) found that using a tuyère and horizontal nozzle distributor the lateral dispersion and lateral mixing in a FBR is significantly improved and reduces the dead zones in the FBR. In the same study a comparison between the dispersion in a bed at different $\frac{U_0 - U_{mf}}{U_{mf}}$ and open-area ratios was done and it was found that the distributors displayed the same trends for these variables.

2.3 Determining the Bubble-Turbulent Regime Transition Boundary (Bi, HT, Ellis & Grace, 2000)

The most commonly used techniques for determining the bubbling-turbulent transition boundary (U_c) are:

1. Visual Observation
2. Local Capacitance
3. Pressure Fluctuations
4. Bed Expansion

Of these methods only the visual observation and pressure fluctuation techniques will be discussed here.

2.3.1 Visual observations

Turbulent fluidizations can be defined as “continuous coalescence - virtually a channelling state with tongues of fluid darting in zigzag fashion through the bed” (Kehoe & Davidson, 1970). Using this definition the bubble-turbulent transition boundary can be defined visually if these conditions are met.

2.3.2 Pressure Fluctuations

Most researchers use the pressure fluctuation method. For this method, both the differential and absolute pressure fluctuations can be used, however it has been shown that the absolute pressure fluctuations are more consistent with the visually observed transition boundary (Bi, HT *et al.*, 2000). Pressure fluctuations have been interpreted using diverse methods such as peak-to-peak amplitude (average or maximum), standard deviation, skewness etc. The transition velocity from the pressure fluctuations has been shown to be consistent with visual observations. Figure 2-2 shows the definition of U_c and U_k , however U_k is rarely used as it is system dependent (Bi, HT, *et al.*, 2000).

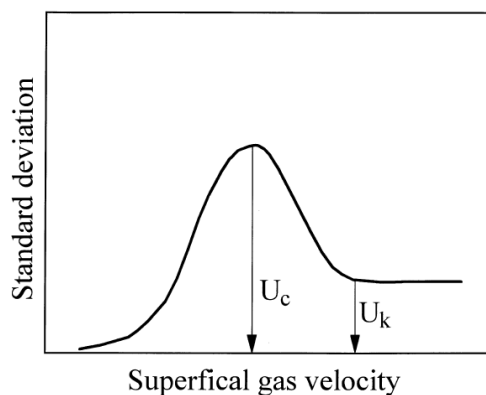


Figure 2-2: The definition of U_c and U_k w.r.t the standard deviation of the absolute pressure fluctuations (Bi, HT *et al.*, 2000).

2.4 ***Pressure Fluctuation Relation to Bubble Size*** ***(Van der Schaaf et al., 2002)***

In FBRs the bubble characteristics are important parameters in quantifying the FBR performance. Bubbles provide mixing of the particles and therefore better heat transfer in the bed. Unfortunately the bubbles provide a “short circuit” for the gaseous reactant through the bed which reduces gas-solid contacting and accordingly reduces the FBR efficiency.

Bubble characteristics can be measured directly using techniques such as optical, capacitance and radioactive methods. The optical and capacitance measurement techniques only provide localized bubble measurements as only a small portion of the bubbles are detected by the probes in the FBR, while radioactive measurement techniques can be very expensive to run and are usually restricted to small scale beds.

Pressure fluctuations caused by rising bubbles can be used as an indirect measure of bubble sizes and velocities. The pressure fluctuations in a FBR are, however, not limited to rising bubbles; other sources include bed mass fluctuations, coalescence of bubbles, eruption of bubbles and turbulence caused by gas.

Differentiating between the pressure fluctuations caused by the bubbles in the bed and other sources of pressure fluctuations can be done by decomposing the pressure time series into its multiple components. The components are caused by different physical phenomena and can therefore be used to identify the physical properties of the FBR.

2.4.1 Decomposing the Pressure Time Series

The power spectral density (PSD) of a pressure time series ($p_x(t)$) is defined by equation 2-1:

$$\Phi_{xx}(f) = \frac{1}{T} \langle \mathcal{F}_x(f) \mathcal{F}_x^*(f) \rangle \quad 2-1$$

The cross power spectral density (Φ_{xy}) of two separate pressure time series measured at position x and y ($p_x(t)$ and $p_y(t)$) are represented by equation 2-2:

$$\Phi_{xy}(f) = \frac{1}{T} \langle \mathcal{F}_x(f) \mathcal{F}_y^*(f) \rangle \quad 2-2$$

The $\Phi_{xy}(f)$ will be high if the time series are coherent for a specific frequency. Due to the dependence of the $\Phi_{xy}(f)$ on the actual power present in the $p_x(t)$ and $p_y(t)$, the $\Phi_{xy}(f)$ is normalized with $\sqrt{\Phi_{xx}(f)\Phi_{yy}(f)}$. The square of the normalization yields the coherence (γ_{xy}^2) which ranges from 0 to 1:

$$\gamma_{xy}^2(f) = \frac{\Phi_{xy}(f)\Phi_{xy}^*(f)}{\Phi_{xx}(f)\Phi_{yy}(f)} \quad 2-3$$

The value of γ_{xy}^2 indicates the correlation between the time series' PSDs. A value of unity indicates that the PSDs are fully correlated (even if the power is not equal) while a value of zero means that they are not coupled (even if the power is equally high). The γ_{xy}^2 between different time series in a FBR can be used to separate the components of the pressure fluctuations.

2.4.2 Components of Pressure Fluctuations in a FBR

The pressure fluctuations in a FBR consist of:

1. Global pressure waves which are measured almost instantaneously throughout the entire bed (including the plenum chamber) which are caused by bubble coalescence, bubble eruptions, gas fluctuations and fluctuations in bed inventory
2. Localized pressure fluctuations which do not propagate axially through the bed, caused by local bubbles and turbulence

The pressure time series measured at a height y above the distributor can therefore be described as a combination of the global pressure fluctuations and the localized pressure fluctuations (equation 2-4):

$$p_y(t) = a_y(t)p_x(t + \Delta) + b_y(t) \quad 2-4$$

The variable $a_y(t)$ quantifies the reduction of the coherent global pressure fluctuations, Δ the time delay of the global pressure waves through the bed and $b_y(t)$ the bubble input to the pressure time series.

The γ_{xy}^2 between the plenum chamber and the position y in the bed indicates the dominance of the global pressure fluctuations on the pressure time series. The power of the coherent or incoherent effect of the fast traveling pressure waves can be expressed by the coherent-output PSD ($COP_{xy}(f)$) and the incoherent-output PSD ($IOP_{xy}(f)$), as shown in equations 2-5 and 2-6 respectively:

$$COP_{xy}(f) = \gamma_{xy}^2 \Phi_{yy} \quad 2-5$$

$$IOP_{xy}(f) = (1 - \gamma_{xy}^2) \Phi_{yy} \quad 2-6$$

The standard deviation of the coherent and incoherent pressure fluctuations can be calculated from the $COP_{xy}(f)$ and $IOP_{xy}(f)$ respectively using equations 2-7 and 2-8 respectively:

$$\sigma_{xy,c}^2 = \int_0^{\infty} COP_{xy}(f) df \quad 2-7$$

$$\sigma_{xy,i}^2 = \int_0^{\infty} IOP_{xy}(f) df \quad 2-8$$

The physical significance of the $\sigma_{xy,c}^2$ and $\sigma_{xy,i}^2$ can be expressed by substituting 2-4 into equations 2-5 to 2-7, which yields equation 2-9:

$$\sigma_{xy,c}^2 = \langle a_y^2(t) p_x^2(t) \rangle = A_y^2 \sigma_x^2 \text{ and } \sigma_{xy,i}^2 = \langle b_y^2(t) p_x^2(t) \rangle = B_y^2 \quad 2-9$$

From equation 2-9 it can be seen that $\sigma_{xy,c}^2$ gives information on the average reduction of the fast pressure waves, but more significantly the $\sigma_{xy,i}$ is directly proportional to the pressure fluctuation amplitude of the rising bubbles, which is in turn propor-

tional to the gas bubble diameter. Therefore the pressure time series can be used for the non-intrusive measurement of the bubble diameter in the FBR.

The $\sigma_{xy,i}$ unfortunately does not measure the bubble diameter quantitatively and needs to be calibrated using a direct measurement technique before it can be used to predict the bubble sizes in the FBR.

2.5 **Modeling Catalytic Fluidized Bed Reactors**

Most bubbling fluidized bed reactor models consider at least two “phases”, i.e. a dilute phase which represents the bubbles in the bed and a continuous dense phase which represents the solids between the bubbles (Abba *et al.*, 2003). Two such models are

1. The Kunii & Levenspiel three-phase model (K-L model) in which the three phases are defined as the emulsion phase, an intermediate cloud phase around the bubble and the bubble phase (Levenspiel, 1999: 455).
2. The Grace two-phase model (G2PM) in which two phases is defined: the low-density phase and the high-density phase (Grace, 1984).

These two models are discussed in the subsequent sections as they have been implemented successfully in simulating the bubbling bed behaviour with proper bubble size estimation (Abba *et al.*, 2003). In addition, a model (Thompson model) which accounts for turbulent bed behaviour in the FBR is discussed. This model uses a probabilistic averaging method to predict the transition from the G2PM to an axially dispersed plug flow model (ADPFM) as the bed moves from the bubbling to the turbulent regime (Thompson, Bi, HT, & Grace, 1999; Abba *et al.*, 2003).

2.5.1 Kunii and Levenspiel Three Phase Model (K-L model) (Levenspiel, 1999: 455)

The model is shown in Figure 2-3.

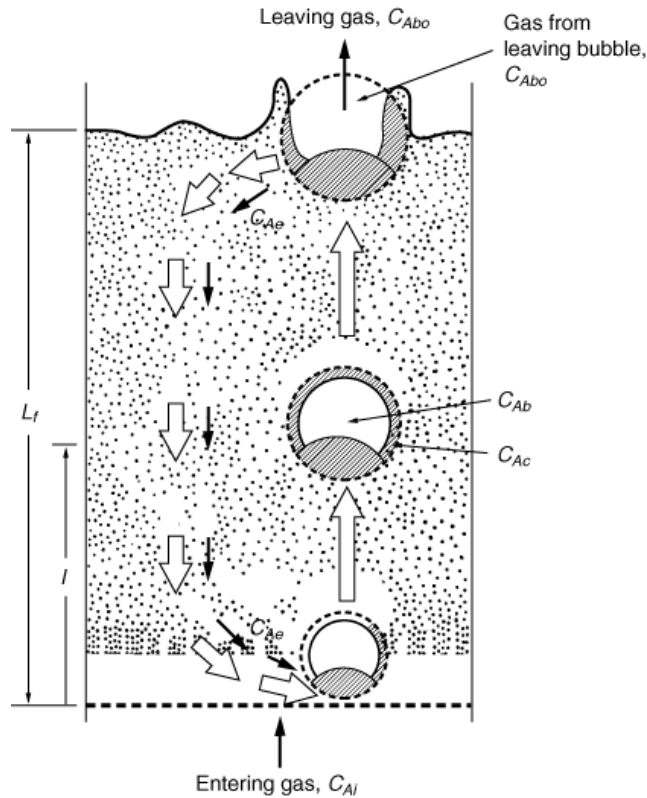


Figure 2-3: The diagrammatic representation of the flow pattern in the BFB for the hydrodynamic description of the K-L model (Fogler, 2006:853)

The K-L model was formulated with the following assumptions:

- The bubbles are all spherical, of same size d_b , and are all surrounded by a thin cloud rising through the dense emulsion phase. The upflow of gas through the cloud is ignored because the cloud is very small compared to the bubble. In this regime $U_b \gg U_e$.
- The emulsion stays at U_{mf}
- The bubbles drag a wake of solids behind them which creates a circulation of solids in the bed.

2.5.1.1 The Mathematic Representation of the K-L Model:

2.5.1.1.1 Material Balances:

$$u_{br} = 0.711(gd_b)^{\frac{1}{2}} \quad 2-10$$

$$U_b = U_0 - U_{mf} + u_{br} \quad 2-11$$

$$\delta = \frac{U_0 - U_{mf}}{U_b} \quad 2-12$$

$$H = \frac{(1 - f_c)M_{s0}}{\rho_s A_c (1 - \epsilon_f)} \quad 2-13$$

2.5.1.1.2 Parameter Estimation

$$K_{bc} = f_{K_{bc}} \left[4.50 \left(\frac{U_{mf}}{d_b} \right) + 5.85 \left(\frac{\mathcal{D}^{\frac{1}{2}} g^{\frac{1}{4}}}{d_b^{\frac{5}{4}}} \right) \right] \quad 2-14$$

$$K_{ce} = f_{K_{ce}} 6.77 \left(\frac{\epsilon_{mf} \mathcal{D} u_{br}}{d_b^3} \right)^{\frac{1}{2}} \quad 2-15$$

$$f_b = 0.001 \sim 0.01 \quad 2-16$$

$$f_{cl} = \delta (1 - \epsilon_{mf}) \left[\frac{3u_{mf}/\epsilon_{mf}}{u_{br} - \frac{u_{mf}}{\epsilon_{mf}}} + \alpha \right] \quad 2-17$$

$$f_e = (1 - \epsilon_{mf})(1 - \delta) - f_{cl} - f_b \quad 2-18$$

If the values for U_{mf} , ϵ_{mf} , U_0 and d_b are known the K-L model predicts other bed properties such as the flows, region volumes, interchange rates and therefore reactor behaviour.

2.5.1.1.3 Catalytic Reactions:

The development by of the K-L model for catalytic reactions is based in the following assumptions:

- The axial flow of the gas through the cloud phase is negligible when compared to the flow through the column as the cloud volume is very small compared to the bubble volume.
- The flow of gas through the emulsion phase stays at minimum fluidization velocity, which for larger overall flows is almost negligible.

The model is shown diagrammatically in Figure 2-4, with the corresponding mathematical model represented in equations 2-19, 2-20 and 2-21:

$$U_b^* \frac{dC_{Ab}}{dz} = -\delta K_{bc}(C_{Ab} - C_{Acl}) - k_r''' f_b C_{Ab}^n \quad 2-19$$

$$U_{cl}^* \frac{dC_{Acl}}{dz} = \delta K_{bc}(C_{Ab} - C_{Acl}) - \delta K_{ce}(C_{Acl} - C_{Ae}) - k_r''' f_{cl} C_{Acl}^n \quad 2-20$$

$$U_e^* \frac{dC_{Ae}}{dz} = \delta K_{ce}(C_{Acl} - C_{Ae}) - k_r''' f_e C_{Ae}^n \quad 2-21$$

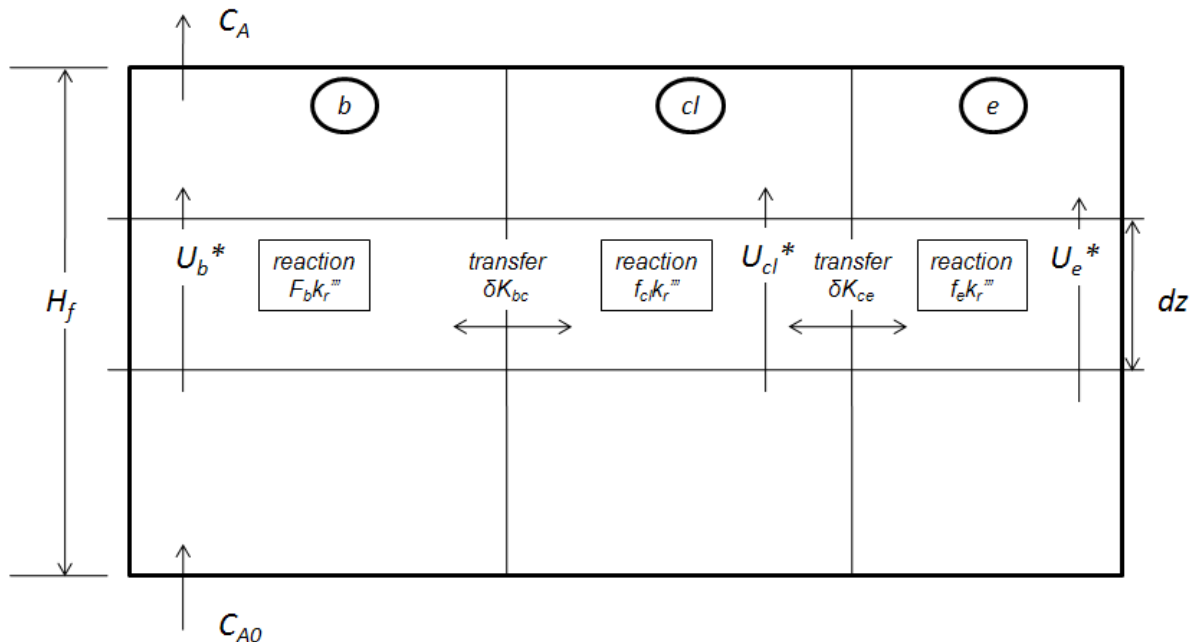


Figure 2-4: Diagrammatic representation of the K-L model with catalytic reaction

2.5.1.2 Model Analysis

The analysis of the K-L model is shown in Table 2-2, which shows that the fitted parameters for the model are α , f_b , $f_{K_{bc}}$ and $f_{K_{ce}}$. The first parameter (α) is a measure of the wake volume to the bubble volume ratio, f_b defines the solid fraction in the bubble phase and the last two parameters ($f_{K_{bc}}$, $f_{K_{ce}}$) are a measure of the mass transfer in the bed.

Table 2-2: K-L Model Analysis

Description	Variables	Equations
Differential species balance	C_{Ab}, C_{Acl}, C_{Ae}	2-19 to 2-21
Material balances	u_{br}, U_b, δ	2-10 to 2-13
Empirical estimation	K_{bc}, K_{ce}, f_c, f_e	2-14 to 2-18
Specified parameters	$U_{mf}, \epsilon_{mf}, k_r''', d_B(U_0), \mathcal{D}, M_{S0}, \rho_S, A_c$	
Fitted Parameters	$\alpha, f_{K_{bc}}, f_{K_{ce}}$	

2.5.2 Grace Two-Phase Bubbling Model (G2PM) (Grace, 1984)

The G2PM is diagrammatically shown in Figure 2-5. The model consists of two-phases present in the FBR (low-density and high-density phases), with axial dispersion present in both phases.

The assumptions for the model are:

- Steady operation.
- Height independent properties.
- Negligible radial variations
- Open-inlet/closed-outlet boundary conditions

2.5.2.1 Mathematical Representation of the G2PM

2.5.2.1.1 Mole Balances

The mole balances for a specific species i are represented by equations 2-22 to 2-24:

$$C_i = q_L C_{i,L} + q_{i,H} \quad 2-22$$

$$u_L \frac{dC_{i,L}}{dz} = D_{z,L} \frac{d^2 C_{i,L}}{dz^2} + \rho_L R_{i,L}(C_L) - k_q a_I \epsilon_L (C_{i,L} - C_{i,H}) \quad 2-23$$

$$u_H \frac{dC_{i,H}}{dz} = D_{z,H} \frac{d^2 C_{i,H}}{dz^2} + \rho_H R_{i,H}(C_H) - \left(\frac{\psi_L}{\psi_H}\right) k_q a_I \epsilon_L (C_{i,L} - C_{i,H}) \quad 2-24$$

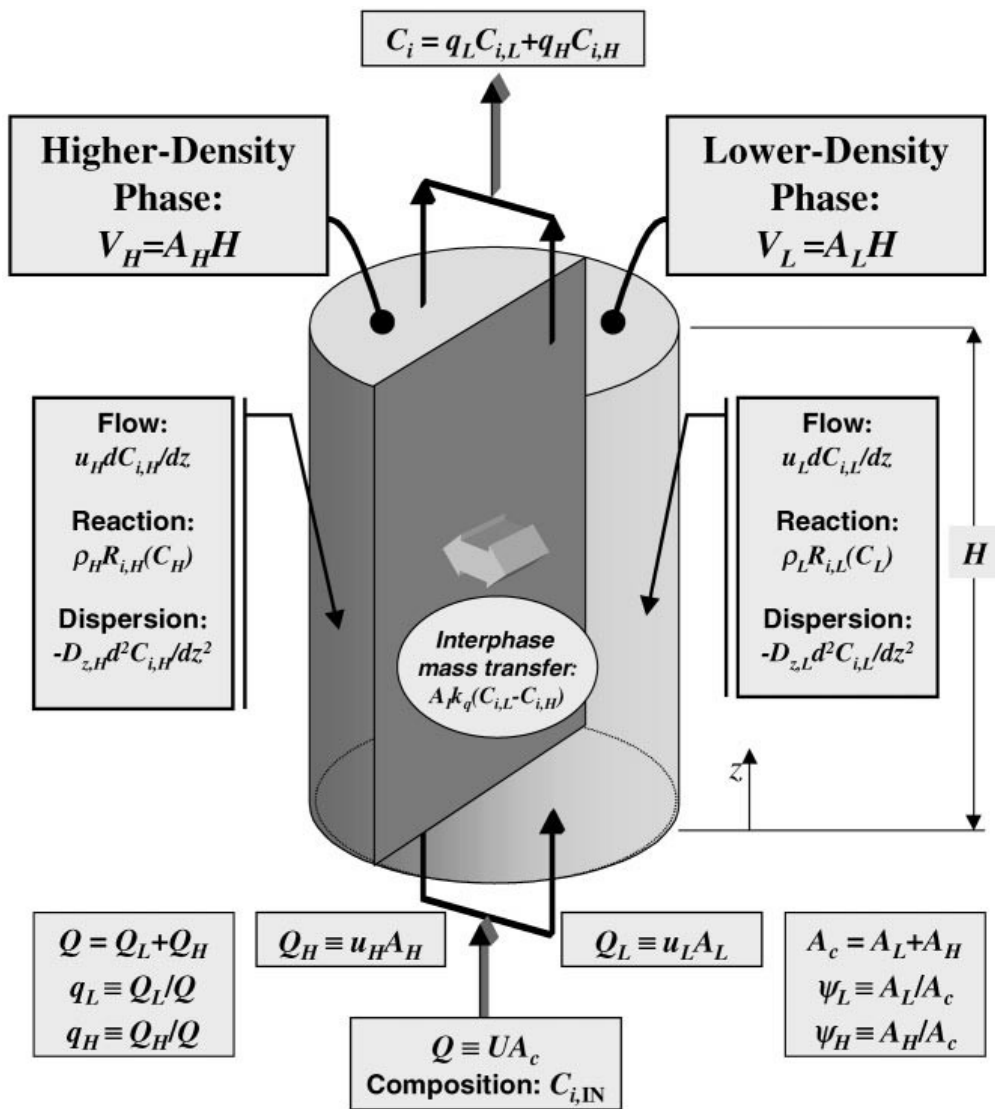


Figure 2-5: The two-phase bubbling model; the inflow (Q) enters from the bottom and separates (Q_H and Q_L). Solid particles and gas are present in both phases, therefore axial dispersion is present in both phases. Interphase mass takes place across interface A_I (Thompson et al., 1999).

The boundary conditions for $z = 0$:

$$u_L (C_{i,L}(0) - C_{i,IN}(0)) = D_{z,L} \left[\frac{dC_{i,L}}{dz} \right]_{z=0}$$

$$u_H (C_{i,H}(0) - C_{i,IN}(0)) = D_{z,H} \left[\frac{dC_{i,H}}{dz} \right]_{z=0}$$

2-25

The boundary conditions for $z = H$:

$$\left[\frac{dC_{i,L}}{dz} \right]_{z=H} = 0, \quad \left[\frac{dC_{i,H}}{dz} \right]_{z=H} = 0,$$

2-26

The reaction rate of species i in which the stoichiometric coefficients v_{ij} conform to:

- $v_{ij} > 0 \forall$ products
- $v_{ij} < 0 \forall$ reagents

$$R_i(\mathbf{C}) = \sum_{j=1}^{N_R} v_{ij} r_j(\mathbf{C})$$

2-27

where: $v_{ij} r_j(\mathbf{C}) = -k_r''' C_i$

2.5.2.1.2 Material Balances

The material balances are represented by equations 2-28 to 2-37:

$$\psi_L + \psi_H = 1$$

$$\left[\psi_L = \frac{V_L}{V}, \psi_H = \frac{V_H}{V} \right]$$

2-28

$$\epsilon_f + \phi_f = 1$$

$$\left[\epsilon_f = \frac{V_G}{V}, \phi_f = \frac{V_S}{V} \right]$$

2-29

$$q_L + q_H = 1$$

$$\left[q_L = \frac{Q_L}{Q}, q_H = \frac{Q_H}{Q} \right] \quad 2-30$$

$$\epsilon_L + \phi_L = 1$$

$$\left[\epsilon_L = \frac{V_{G,L}}{V}, \phi_L = \frac{V_{S,L}}{V} \right] \quad 2-31$$

$$\epsilon_H + \phi_H = 1$$

$$\left[\epsilon_H = \frac{V_{G,H}}{V}, \phi_H = \frac{V_{S,H}}{V} \right] \quad 2-32$$

$$m_{G,L} + m_{G,H} = 1$$

$$\left[m_{G,L} = \frac{V_{G,L}}{V_G} = \frac{\psi_L \epsilon_L}{\epsilon}, m_{G,H} = \frac{V_{G,H}}{V_G} = \frac{\psi_H \epsilon_H}{\epsilon} \right] \quad 2-33$$

$$m_{S,L} + m_{S,H} = 1$$

$$\left[m_{S,L} = \frac{V_{S,L}}{V_S} = \frac{\psi_L \rho_L}{\rho}, m_{S,H} = \frac{V_{S,H}}{V_S} = \frac{\psi_H \rho_H}{\rho} \right] \quad 2-34$$

$$\rho_L = \rho_s \phi_{Lo} \quad 2-35$$

$$\epsilon_H = \epsilon_{mf} \quad 2-36$$

$$D_{z,L} = \mathfrak{D} \quad 2-37$$

2.5.2.1.3 Parameter Estimation

The parameters estimation equations for the G2PM are shown in equations 2-38 to 2-45:

$$u_L = U_b = (U_0 - U_{mf}) \left(1 + \frac{0.711}{U_0} \sqrt{g d_b} \right) \quad 2-38$$

$$\psi_L = \frac{\epsilon - \epsilon_{mf}}{1 - \phi_{Lo} - \epsilon_{mf}} \quad 2-39$$

$$\epsilon = 1 - \frac{1 - \epsilon_{mf}}{1 + \frac{U - U_{mf}}{0.711 \sqrt{g d_b}}} \quad 2-40$$

$$U_{mf} = \frac{\mu_G}{\rho_G d_p} \left(\sqrt{27.2^2 + 0.0408 Ar} - 27.2 \right) \quad 2-41$$

$$k_q = f_{kq} \left(0.4 U_{mf} + 2 \sqrt{\frac{D \epsilon_{mf} U_b}{\pi d_b}} \right) \quad 2-42$$

$$A_l = \frac{6}{d_b} \quad 2-43$$

$$Pe = \frac{UH}{D_z} = f_{Pe} Ar^{0.32} \left(\frac{D_t}{d_p} \right)^{0.02344} Sc^{-0.2317} \left(\frac{H}{D_t} \right)^{0.2854} \quad 2-44$$

$$D_{z,H} = D_z \quad 2-45$$

2.5.2.2 G2PM Analysis

The analysis of the G2PM is shown in Table 2-3, which shows that the fitted parameters for the model are ϕ_{Lo} , f_{kq} and f_{Pe} . The first parameter is a measure of the solid volume fraction in the lean phase, while the latter two parameters are a measure of the mass transfer in the bed and the turbulence or mixing in the bed, respectively.

A higher value for f_{kq} would indicate a higher interphase mass transfer in the bed. A higher f_{Pe} would indicate a smaller degree of mixing or turbulence in the bed and more PFR-like behaviour present in the bed.

Table 2-3: G2PM Analysis

Description	Variables	Equations
Differential species balance	$C_i, C_{i,L}, C_{i,H}$	2-22 to 2-27
Material balances	$\psi_{\frac{L}{H}}, \epsilon, \phi, q_{\frac{L}{H}}, \epsilon_{\frac{L}{H}}, \phi_{\frac{L}{H}}, m_{G,\frac{L}{H}}, m_{S,L/H}$	2-28 to 2-34
U_0 dependent properties	$\rho_L, \epsilon_H, D_{z,L}$	2-35 to 2-37
Empirical estimation	$u_L, \epsilon, Pe, k_q, U_b, U_{mf}, D_{z,H}$	2-38 to 2-45
Specified parameters	$k_r''' C_i, V, d_B(U_0), \mathcal{D}, \rho_s, \epsilon_{mf}, \mu_G, \rho_G$ and d_p	
Fitted Parameters	$\phi_{Lo}, f_{kq}, f_{Pe}$	

2.5.3 Thompson Model (Thompson *et al.*, 1999; Abba *et al.*, 2003)

Normally turbulent fluidization can be grouped into two distinct categories (Bi, HT, Grace & Lim, 1995):

- Type I: Geldart A type solids with a sharp transition between the bubbling and turbulent regime. Small transient voids criss-cross the bed while the solids are moved at slanted angles upwards or fall back downwards
- Type II: Geldart B/D particle beds in which the fluidizing behaviour alternates intermittently between periods of flow and fast fluidizing behaviour

Modelling FBRs operating in the turbulent regime, four different approaches have been adopted:

1. Empirical relations
2. Single phase plug flow model
3. Axially dispersed single phase plug flow model (ADPFM)
4. Two phase model (G2PM) with increased interphase mass transfer and decreased bubble sizes.

The abovementioned approaches are not very satisfactory individually as the turbulent bed still displays some two-phase behaviour, even though the contacting in the bed is significantly better than the purely bubbling bed. For this reason the single phase plug flow as well as the ADPFM does not predict the fluidizing behaviour sufficiently well.

The Thompson model is a hybrid between the two phase bubbling model and the ADPFM. The model predictions are an interpolation using probabilistic averaging of model parameters between two limiting cases – the purely bubbling fluidized bed and the single phase bed with axial dispersion.

The lower limit of the Thompson model is obtained from the Grace two-phase model with axial dispersion in both phases, which has already been discussed in section 2.5.2. The upper limit of the Thompson model is the ADPFM which is described in the subsequent section.

2.5.3.1 Single Phase Axially Dispersed Plug Flow Model (ADPFM)

In this model the mole balances are taken over a single phase and therefore no interphase mass transfer terms are present. This model is much less involved than the previous two and will only be discussed briefly.

The mole balance for species i :

$$U_0 \frac{dC_i}{dz} = D_z \frac{d^2 C_i}{dz^2} + \phi \rho_s R_i(C) \quad 2-46$$

The boundary conditions at $z = 0$:

$$U_0(C_i(0) - C_i(0)) = D_z \left[\frac{dC_i}{dz} \right]_{z=0} \quad 2-47$$

The boundary conditions at $z = H$:

$$D_z \left[\frac{dC_i}{dz} \right]_{z=0} = 0 \quad 2-48$$

It can be seen that the parameters used to solve this model are $D_z(U_0)$ and $\rho(U_0)$. Equations 2-49 to 2-52 give correlations for these parameters from literature:

$$D_z(U_0) = \frac{U_0 H}{Pe} \quad 2-49$$

with:

$$Pe = f_{pe} Ar^{0.32} \left(\frac{D_t}{d_p} \right)^{0.02344} Sc^{-0.2317} \left(\frac{H}{D_t} \right)^{0.2854}$$

$$(1 - f_c) M_{s0} = \rho_s \phi H A_c \quad 2-50$$

$$\phi = 1 - \epsilon_f \quad 2-51$$

$$\epsilon_f = 1 - \frac{1 - \epsilon_{mf}}{1 + \frac{U - U_{mf}}{0.711 \sqrt{g d_b}}} \quad 2-52$$

From the ADPFM it can be seen that the model can be solved as long as the following bed parameters are known: $Ar, Sc, M_{s0}, \rho_s, A_c, \epsilon_{mf}, U_{mf}, d_b(U_0)$ and the value for f_{pe} are fitted to the experimental results. As in section 2.5.2.2 the variable f_{pe} is a measure of the mixing in the FBR and can therefore be used to qualitatively estimate the mixing of the bed.

2.5.3.2 G2PM and ADPFM Convergence

The Thompson model acts as a merging of the two limiting case models, which entails the varying of the model parameters so that the G2PB model converges to an ADPFM as $U \rightarrow U_\infty$. Equations 2-53 to 2-55 show the mathematical manipulation to achieve this:

Differentiating equation 2-22:

$$\frac{dC_i}{dz} = q_L \frac{dC_{i,L}}{dz} + q_H \frac{dC_{i,H}}{dz} = \frac{1}{U} \left(\psi_L u_L \frac{dC_{i,L}}{dz} + \psi_H u_H \frac{dC_{i,H}}{dz} \right) \quad 2-53$$

Therefore:

$$U \frac{dC_i}{dz} = \alpha_D(z) D_Z \frac{d^2 C_i}{dz^2} + \alpha_{R,i}(z) \rho R_i(C) \quad 2-54$$

Where:

$$\alpha_D(z) \equiv \frac{\psi_L D_{z,L} \frac{d^2 C_{i,L}}{dz^2} + \psi_H D_{z,H} \frac{d^2 C_{i,H}}{dz^2}}{D_z \frac{d^2 C_i}{dz^2}}$$

and

2-55

$$\alpha_{R,i}(z) \equiv \frac{\psi_L \rho_L R_{i,L}(C_L) + \psi_H \rho_H R_{i,H}(C_H)}{\rho R_i(C)}$$

From the mathematical manipulation it can be seen that the G2PM converges to the ADPFM in the limit $U_0 \rightarrow U_\infty$ if (equation 2-56):

$$\lim_{U_0 \rightarrow U_\infty} \alpha_D = 1$$

and

2-56

$$\lim_{U_0 \rightarrow U_\infty} \alpha_{R,i} = 1$$

To satisfy the limits in equation 2-56 the concentration profiles, density and dispersion (C_i , ρ and D_z) must converge to identical values. To satisfy these prerequisites the following limiting equations (2-57 to 2-59) must be satisfied:

$$\lim_{U_0 \rightarrow U_\infty} u_L = \lim_{U_0 \rightarrow U_\infty} u_H = U_0 \quad 2-57$$

$$\lim_{U_0 \rightarrow U_\infty} D_{z,L} = \lim_{U_0 \rightarrow U_\infty} D_{z,H} = D_z \quad 2-58$$

$$\lim_{U_0 \rightarrow U_\infty} \rho_L = \lim_{U_0 \rightarrow U_\infty} \rho_H = \rho \quad 2-59$$

The quantities in equations 2-57 to 2-59 are extremely difficult to measure and therefore a probabilistic approach is taken to predict how these variables approach the limits. Equations 2-60 to 2-62 show the transition equations to express u_L , $D_{z,L}$ and ϕ_L as functions of U_0 . (Note: $\phi_L = \frac{\rho_L}{\rho_s}$)

$$u_L = (1 - P_T(U_0))U_b(U_0) + P_T(U_0)U_0 \quad 2-60$$

$$D_{z,L} = (1 - P_T(U_0))\mathfrak{D} + P_T(U_0)\frac{U_0 H}{Pe(U_0)} \quad 2-61$$

$$\phi_L = (1 - P_T(U_0))\phi_{L_0} + P_T(U_0)\phi(U_0) \quad 2-62$$

And finally a volume balance can be done by limiting the porosities of the bed to:

$$\epsilon_{H,B} = \epsilon_{mf} \text{ and } \epsilon_{H,T} = \epsilon$$

the volume balance yields

$$\psi_L = \frac{\epsilon - \epsilon_{mf}}{1 - \phi_{L_0} - \epsilon_{mf}}$$

2-63

2.5.3.3 Implementation of the Thompson Model

According to Abba *et al.* (2003) the most applicable probability density function (pdf) for the calculation of P_B is the gamma function, represented by equation 2-64 furthermore P_T can be calculated from equation 2-65.

$$P_B = 1 - [1 + e^{-\beta v_c^*}]^{-1}$$

with

$$v_c^* = \frac{(U_0^* - U_{min}^*) - U^*}{\sigma_c^*}$$

2-64

$$P_T = 1 - P_B$$

2-65

$$U_c^* = \frac{Re_c}{Ar^{\frac{1}{3}}} \text{ and } U_{c,exp,j}^* = \frac{Re_{c,exp,j}}{Ar^{\frac{1}{3}}}$$

2-66

From equations 2-64 and 2-65 it can be seen that the probability that the bed is in either the bubbling or turbulent regime, can be calculated from knowledge of the bubble turbulent transition boundary (U_c) and the variance in the uncertainty of the transition boundary (σ_c^*).

The implementation of the Thompson model requires the fitting of f_{kq} and f_{pe} (the same as for the G2PM). The significance of the fitted parameters is:

- f_{kq} is a measure of the interphase mass transfer present in the bed. This parameter plays the greatest role in the bubbling regime where phase separation has a dominant effect on the reactor performance
- f_{pe} is a measure of the mixing or turbulence in the bed and is most significant in the turbulent regime where the mixing and consequently axial dispersion in the bed affects the reactor performance. The higher the value for f_{pe} the closer to plug flow behaviour of the bed.

3 Experimental setup

3.1 *Equipment*

3.1.1 Fluidized bed Reactor

The reactor used for the experimental study was a Plexiglas two-dimensional (2-D) fluidized bed reactor with the following dimensions:

- Thickness: 25 mm
- Width : 400 mm
- Height: 4.5 m

The primary cyclone is a volute cyclone, required due to high solids loading at the upper gas velocities of the study, and the secondary cyclone a tangential cyclone. Excess fines that bypassed the secondary cyclone were captured in filter bags connected after the secondary cyclone. Saayman (2009) includes the complete engineering drawings for the reactor. Figure 3-1 shows the piping and instrumentation for the experimental setup. The volumetric flow of reactor feed gas was controlled with a vortex flow meter with a linear velocity range of between 0.1 m/s and 0.6 m/s.

The pressure across the distributor and the cyclones was measured using differential pressure meters from Rosemount Analytical. Two pressure transmitters (Wika S-10, Range 0-1.6 barg, maximum measurement frequency of 1000Hz) were connected to the column; at the surface of the distributor and at a height of 0.3 m above the distributor.

Air was used to fluidize the bed and was supplied by a compressor with a chiller which kept the temperature into the bed at a constant 15°C. Prior to introduction into the bed, the air was dosed with ozone generated using the EcoTec MZV1000 cold corona ozone generator (maximum dosing 1g/l). For the generation of the ozone, pure oxygen was used, instead of air, to reduce the possibility of NO_x gasses forming in the ozone generator.

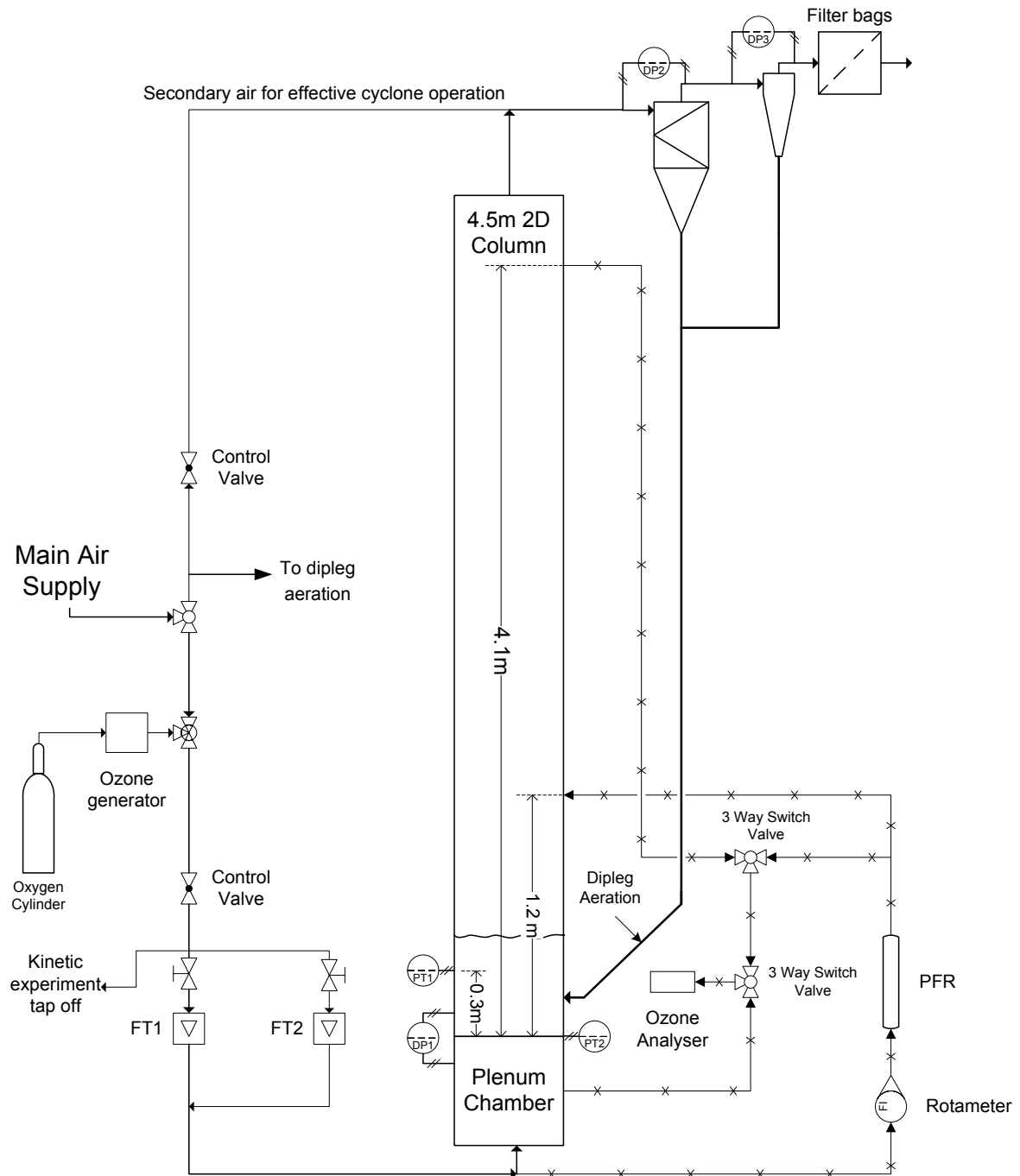


Figure 3-1: The piping and instrumentation for the experimental setup adapted from (Saayman, 2009).

The ozone inlet concentration was determined by sampling the air in the plenum chamber. A UV-106 ozone analyser from 2B Technologies Inc. were used for the analysis. The ozone concentration was measured by light absorption at a wavelength of 254nm. A sampling probe, inserted into the centre of the plenum chamber, was used to withdraw the sample. Glass beads were placed in the plenum chamber

to ensure proper air-ozone mixing. The outlet ozone concentration was measured by drawing a sample from the centre of the reactor, at a height of 4.1m above the distributor. The sample flow rates were negligible when compared to the total column flow rate. The inlet and outlet ozone concentrations were individually measured; only one ozone analyser was available.

3.1.1 Packed Bed Reactor (PBR)

Connected in parallel to the reactor, was a small packed bed reactor::

- Height: 50 mm
- Inner diameter: 16.4 mm
- Catalyst loading: Approximately 10g

and was used to:

- check the deactivation of the catalyst, as operation could only commence after the stable period of operation was reached;
- continuously monitor the catalyst activity

The connection of the PBR to the column is shown in Figure 3-1.

3.1.2 Distributors

The distributors used in the experimental setup were:

- A triangular pitch perforated plate distributor with 35 x 2 mm holes, with a porous cloth between the plenum chamber and the distributor, to prevent weepage. The cloth also increased the pressure drop over the distributor and therefore the gas distribution over the distributor.
- A multi-vortex (MV) distributor consisting of 38 x 1/16" OD tuyères, with triangular pitch, ejecting gas either horizontally or vertically in strategic directions.

Figure 3-2 shows a photograph as well as an isometric representation of the MV distributor used in the experimental study. The mechanical drawing and dimensions are shown in Appendix C.

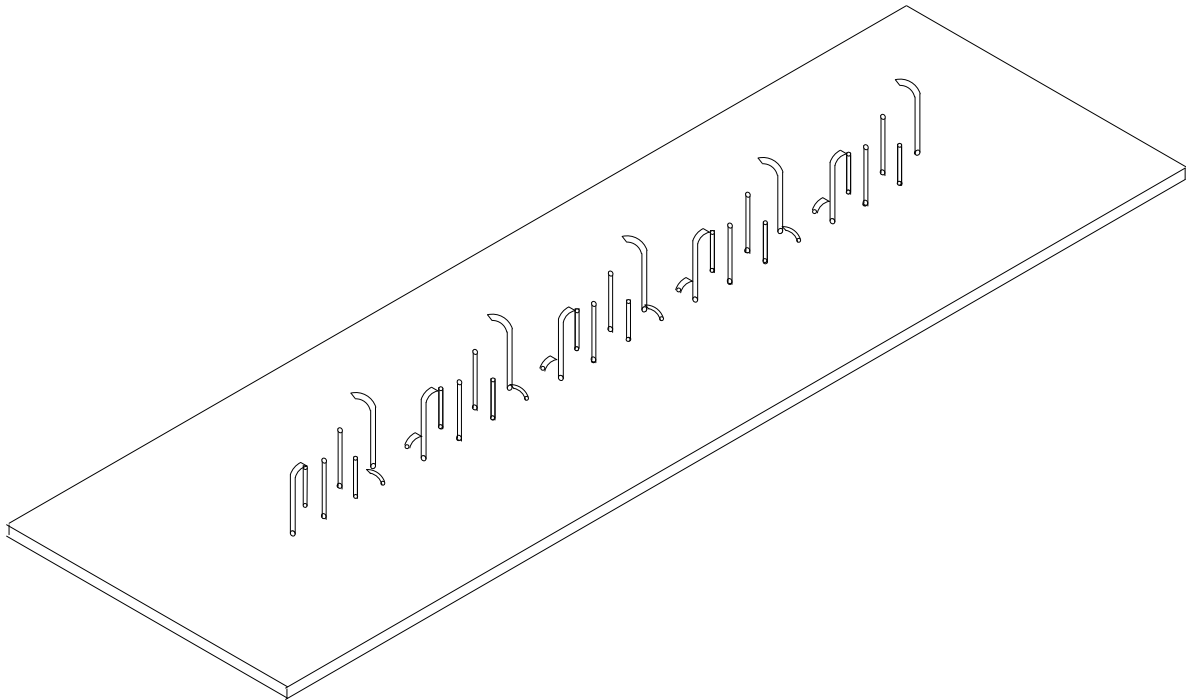
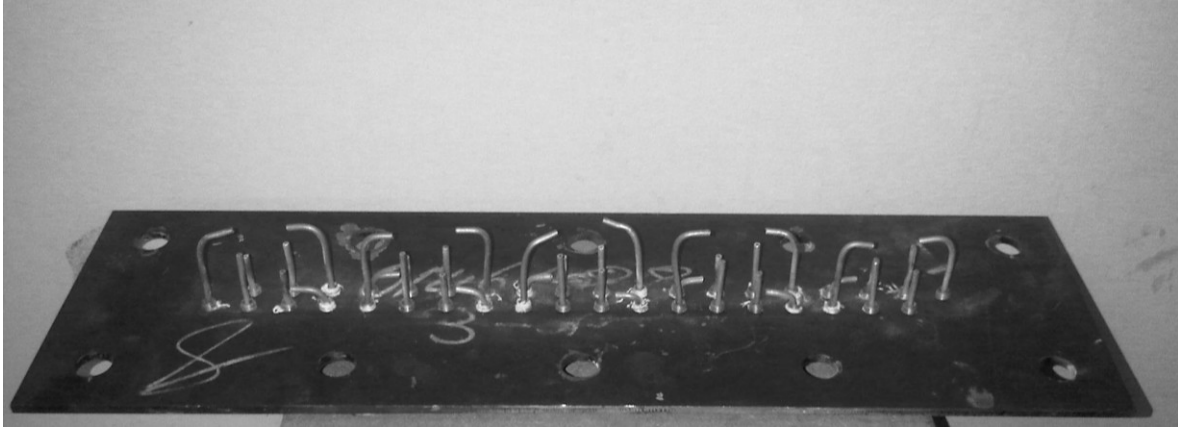


Figure 3-2: Photograph and isometric representation of the MV distributor

The MV distributor was designed to improve the horizontal mixing in the FBR by inducing localized vortices around five distinct sets of nozzles. Figure 3-3 shows the proposed gas flow pattern in each case. As can be seen from Figure 3-3 the proposed vortices at the distributor surface would increase the horizontal momentum at the surface of the distributor, thereby increasing the mixing on the surface of the distributor. This would in turn increase the lateral dispersion in the FBR, increase the mass transfer in the bed and decrease the formation of dead zones on the surface of the distributor (Section 2.2.2 on page 2-4).

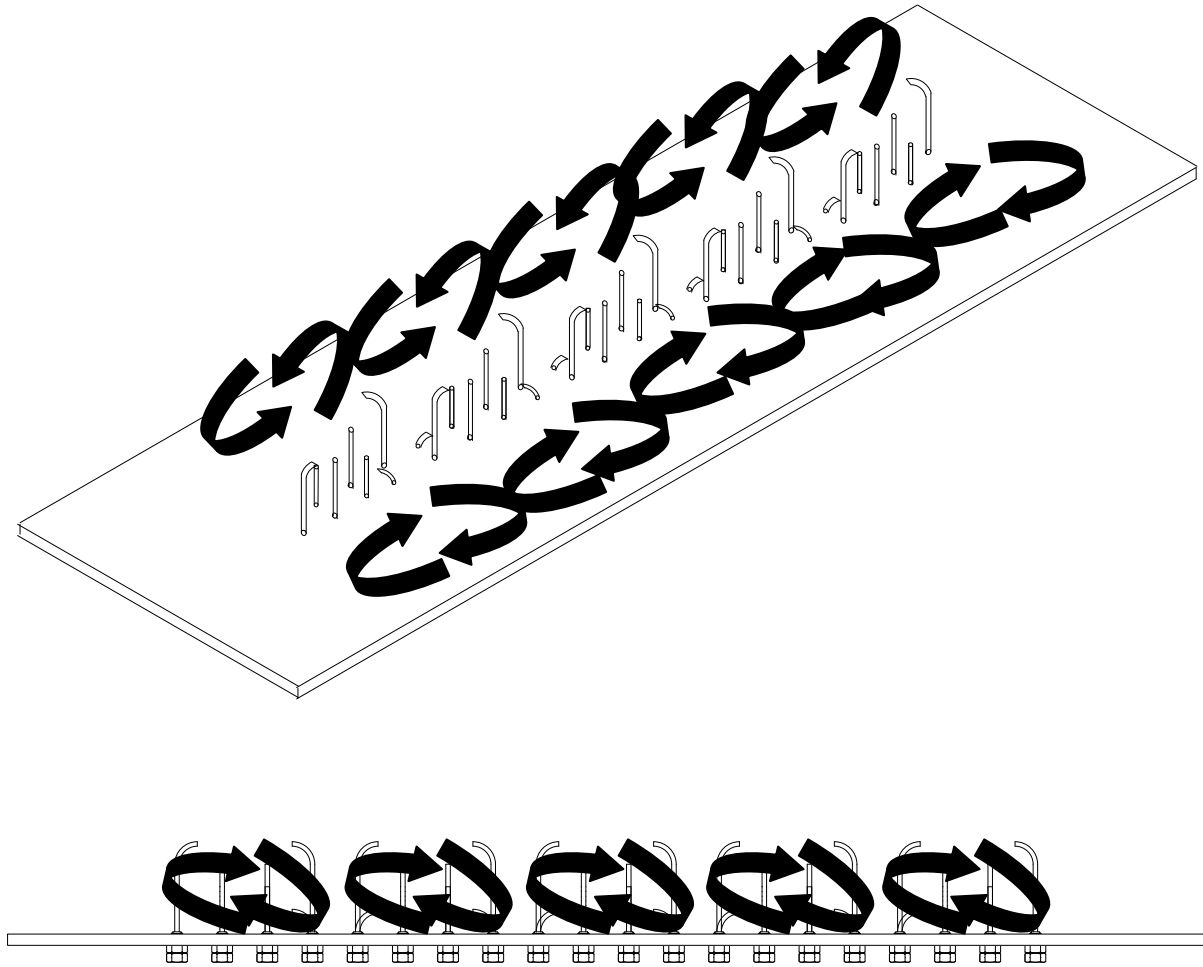


Figure 3-3: Isometric and front-view representation of the gas flow pattern of the MV distributor during operation

The conduit sizing for the MV distributor was chosen to have an equal open area for gas injection for both the baseline and MV distributors. The calculated open area and ratio of orifice velocities to superficial velocity are shown in Table 3-1:

Table 3-1: Comparative Distributor Characteristics for the Experimental Study

	Baseline Distributor	MV Distributor
$ID (mm)$	1.9	1.755
$A_{or}(mm^2)$	2.84	2.42
N_{or}	35	38
$A_{open}(mm^2)$	99	92
$\frac{U_{or}}{U_o}$	101	109

The pressure drop for both distributor designs was increased so as to be much greater than the pressure drop over the bed, ensuring thorough distribution. This was done by inserting a porous cloth below the baseline distributor and by inserting glass wool into the nozzles of the MV distributor. Additionally these measures prevented weepage of solid from the bed into the plenum chamber.

3.1.3 Visible Bubble Size Measurements

For the visible bubble size measurements a 12.1 megapixel digital camera (Sony Cybershot DSCW230 12.1MP) was used, with a frame rate of 30 fps. A standard 300 mm ruler, marked at 10mm intervals was fixed to the column as a reference. Data analysis was done visually and logged in Microsoft® Excel 2007.

3.1.4 Data Acquisition

Data acquisition was done using National Instruments USB-6008 analogue signal data loggers connected to a PC. All the instrumentation had a signal output of 4mA – 20mA over their range. The readings from the ozone analyser were measured at a rate of 5Hz, the velocity measurements were logged at a rate of 20Hz and the pressure fluctuations at a rate of 200Hz.

3.2 Catalyst Preparation

The catalyst in this study was produced by adding the FCC catalyst (support particle) to a mixture of 10% (wt) Ferric Nitrate solution. After stirring for one hour the mixture was calcinated at 450 °C for approximately 1.4 hours, during which the NO₂ gasses were released from the mixture (Saayman, 2009).

3.2.1 Catalyst Activity

The PBR was used to measure the catalyst activity. Using the Pe_r correlation from (Fogler, 2006: 958) shown in equation 3-1:

$$Pe_r = \frac{U_0 L}{D} \quad 3-1$$

the Pe_r number was calculated as 613 for the range of velocities studied (0.02m/s to 0.15m/s) with the dispersion term $D = 1.4 \times 10^{-6} \frac{m}{s}$ to $1.2 \times 10^{-5} \frac{m}{s}$ (Levenspiel,

1999:311). This proves that the PBR acts as a plug flow reactor (PFR) for all velocities used.

According to the literature (Sun & Grace, 1990; Ouyang, S, Lin, J & Potter, 1993; Zimmermann & Taghipour, 2005; Fan *et al.*, 2008; Schoenfelder, Kruse & Werther, 1996; Pagliolico *et al.*, 1992), the ozone decomposition reaction follows first order power law kinetics towards the ozone concentration, therefore the generalized PFR equation (equation 3-2) for first order kinetics was used to determine the reaction rate constant (k_r''').

$$\frac{dx}{d\tau} = k_r'''(1 - x) \quad 3-2$$

with:

$$\tau = \frac{V_{cat}}{Q}$$

To measure the catalyst activity, a known mass of catalyst (approximately 10g) was taken from the bed at start up. A typical $x - \tau$ curve used to fit the reaction rate constant in equation 3-2 is shown in Figure 3-4.

The catalyst activity was measured periodically over time until the catalyst stabilized. This was done initially in the presence of ozone to determine the effect of ozone on the deactivation time and final activity of the catalyst. The deactivation profile is shown in Figure 3-5. From this curve it can be seen that the catalyst deactivates to a stable value in about two hours, in this case with a mean final $k_r''' \approx 1.6 \text{ s}^{-1}$.

Due to the high usage of pure oxygen for this method of deactivation the deactivation was attempted using air in the absence of ozone. Air was fed to the PBR for a period of 2 hours, after which the activity and stability of the catalyst was tested in the PBR as well as the FBR. The catalyst deactivation was found to be independent of ozone in the feed gas as the final activity of the catalyst stabilized at close to the same catalyst activities ($k_r''' = 1.3 \text{ s}^{-1} - 1.6 \text{ s}^{-1}$).

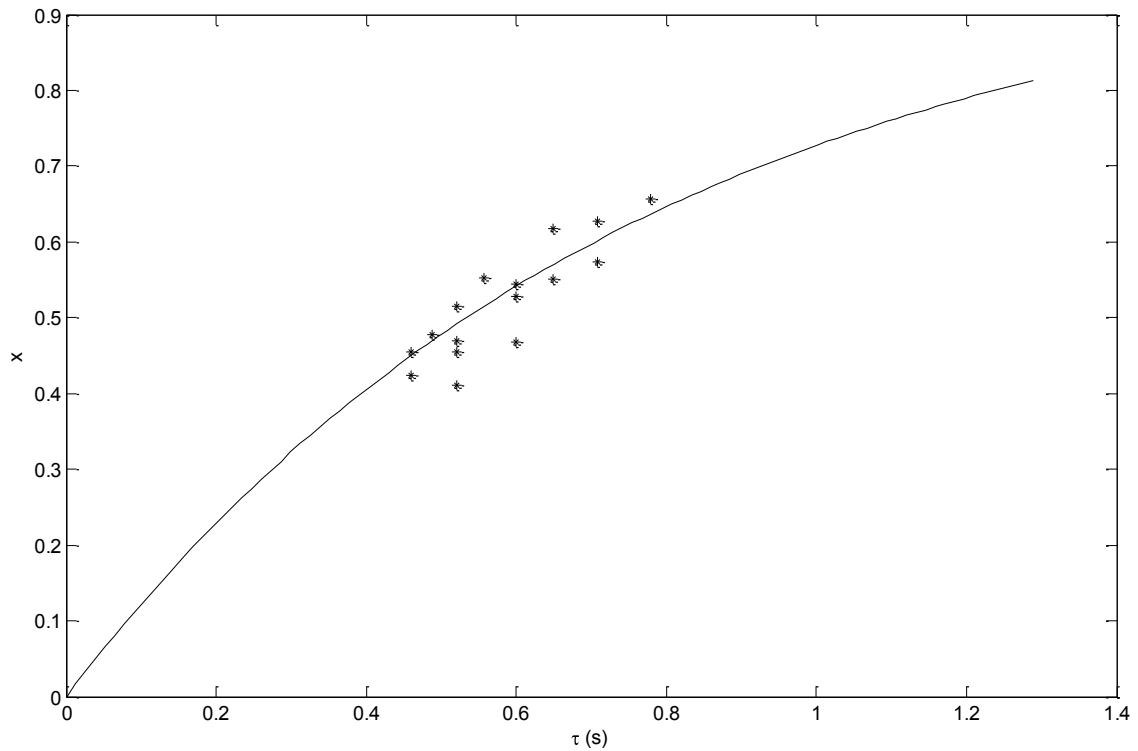


Figure 3-4: A typical fit (equation 3-2) for the reaction rate constant k_r''' . In this case the $k_r''' = 1.3 \text{ s}^{-1}$, which demonstrates the first order kinetics towards ozone concentration in the PBR.

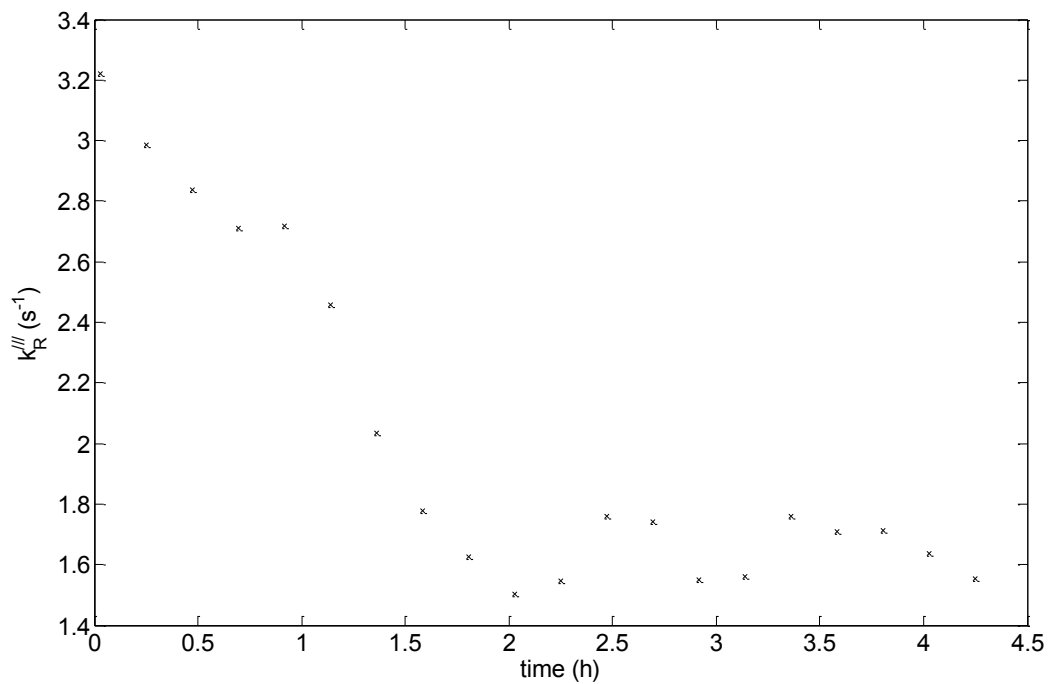


Figure 3-5: Typical curve for the deactivation of the catalyst over time.

Intermittent samples (about 10g of catalyst) were taken from the bed and the activity measured in the PBR to ensure that the activity of the catalyst in the bed remained constant and stable. The catalyst activity was found to remain relatively constant throughout any specific experimental run (the runs lasted between 6h and 12h each, after deactivation); Figure 3-6 shows the $\tau - x$ profiles for a single experimental run at different times during the experiment. It can be seen that the measured catalyst activity fluctuates between $k_r''' = 1.2 \text{ s}^{-1}$ to 1.8 s^{-1} for the entire experiment. The deviation can be explained by the fluctuation in catalyst activity as seen in Figure 3-5 from time $t \geq 2h$. It was decided to use an average k_r''' for each experimental run, determined from the $\tau - x$ profiles (e.g. Figure 3-6)

The catalyst particle size distribution did not vary significantly for the experiments performed using both distributors. The particle size distributions measured in a Melvern® Mastersizer particle size analyser are shown in Figure D-1 and Figure D-2 in Appendix D.

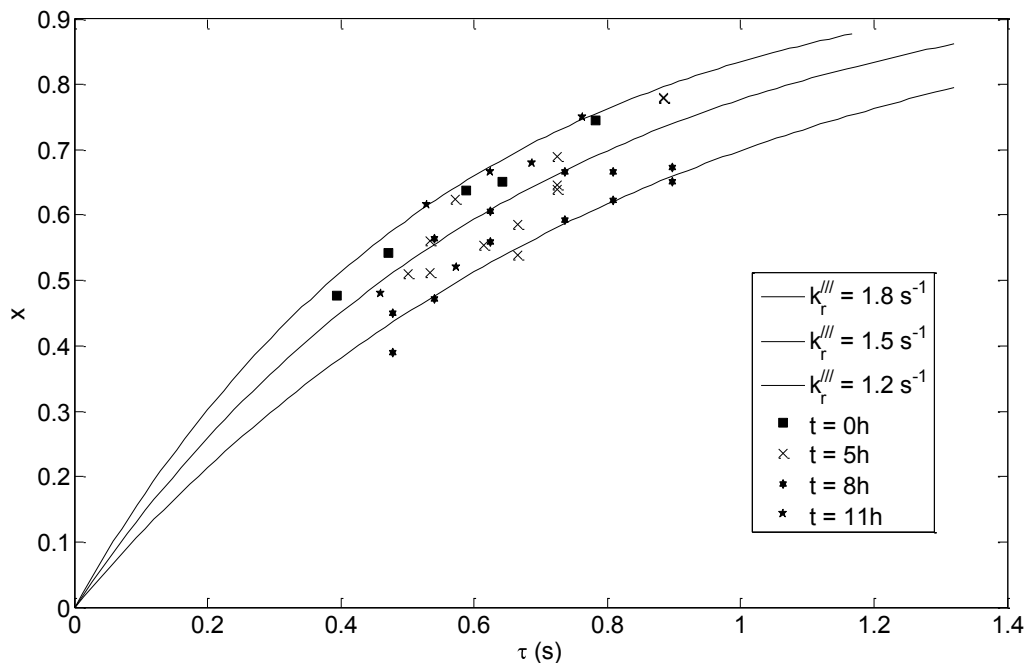


Figure 3-6: A typical $\tau - x$ curve over at different times during an experimental run. The time $t = 0h$ represents the time after deactivation i.e. 2h after start-up.

3.3 **Method**

Initially 3.75 kg of catalyst was loaded to the reactor. It was estimated that 0.75 kg of catalyst remained in the return system and did not take part in the chemical reaction; no ozone was present in the fluidizing gas flow to the dipleg. The bed height prior to fluidization was in the order of 400 mm.

3.3.1 FBR Ozone Measurements

For the FBR ozone measurements:

1. The linear inlet velocity was adjusted to the desired velocity, between 0.1 m/s-0.35 m/s.
2. The ozone inlet concentration was adjusted to between 20 ppm-100 ppm.
3. The inlet ozone concentration was logged for 10 min to account for variations in the ozone concentration. The analyser feed was then changed to the outlet ozone concentration which logged for 10 min in turn.

The variation in measured ozone concentration was accounted for in the conversion calculation using equations 3-3 and 3-4:

$$x = \frac{\text{mean}(C_{\text{ozone,IN}}) - \text{mean}(C_{\text{ozone,OUT}})}{\text{mean}(C_{\text{ozone,IN}})} \quad 3-3$$

$$\sigma_x^2 = \frac{\sigma_{\text{ozone,IN}}^2 - \sigma_{\text{ozone,OUT}}^2}{\sigma_{\text{ozone,IN}}^2} \quad 3-4$$

3.3.2 Visual Bubble Size Analysis

The column was filmed for a period of 30s, with the camera mounted at the ruler height. The linear velocities in both distributor configurations ranged from 0.1 m/s to 0.35 m/s in intervals of 0.05 m/s. A typical range of frames taken at a velocity 0.20 m/s, using the MV distributor is shown in Figure 3-7.

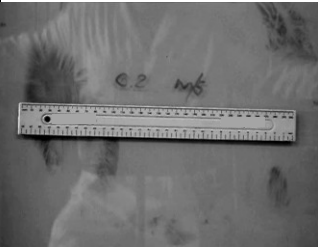
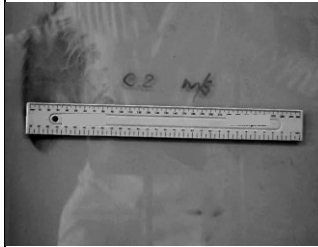
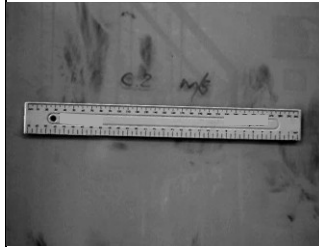
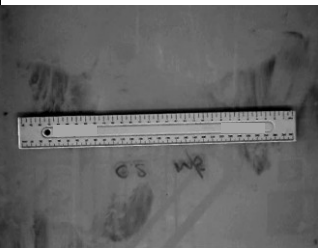


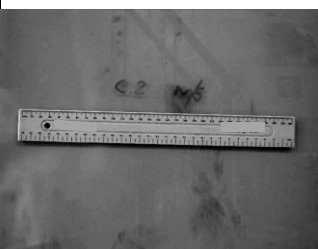


Time (s)		Time (s)		Time (s)	
0.03		0.07		0.1	
0.13		0.17		0.2	
0.23		0.27		0.3	

Figure 3-7: Typical range of snapshots of the bubble sizes taken ($U_o = 0.2$ m/s, MV distributor).

A total of 50 snapshots were taken for each velocity and the bubble sizes were averaged to determine the mean bubble size of each.

4 Results and Discussions

4.1 Ozone Measurements

Due to the daily variation in the activity of the catalyst in the FBR, it was decided to report the conversion efficiency instead of the actual conversion. This would cancel the effect of the activity of the catalyst and thereby normalize the results. The conversion efficiency (x/x_{PFR}) is defined as the ratio of the measured or predicted conversion to the conversion in an ideal PFR with the same activity and retention time as the FBR.

The experimental results for the original perforated plate distributor (baseline) as well as the newly designed distributor are shown in Figure 4-1. The experimental results exhibited some scatter due to experimental error as a result of non-ideal mixing of the gas in the FBR plenum chamber and the freeboard where the measurements were taken, the fluctuations in ozone generation, gas flow fluctuations from the compressor as well as fluctuations in the ozone sensor. The error bars show one standard deviation from the average measured conversion, taken over the experimentally determined ozone measurements.

As can be seen in Figure 4-1, there seems to be quite extensive scatter in the measured conversion efficiency, yet a prominent trend is exhibited in both cases. A very definite dip in the conversion efficiency takes place from 0.1 m/s to approximately 0.3 m/s. This corresponds well to the measured results from Saayman (2009). To refine the results, i.e. filter the scatter to a more manageable trend, a moving average over 5 consecutive data points was applied to the data. An average was taken over a set of five consecutive data points after which the set was moved forward repeating the process. The result of the averaging of the data is shown in Figure 4-2.

Figure 4-2 shows a definite increase in the conversion efficiency when using the MV distributor as compared to the baseline distributor. Figure 4-3 shows the percentage increase of the conversion efficiency for the new distributor. This increase varies between 0% and 20 %, with a mean improvement of 14.7%. What is quite notable about the improvement is that above a linear velocity of 0.2 m/s the percentage im-

provement remains relatively equally spread about the mean and doesn't drop below a 10% improvement.

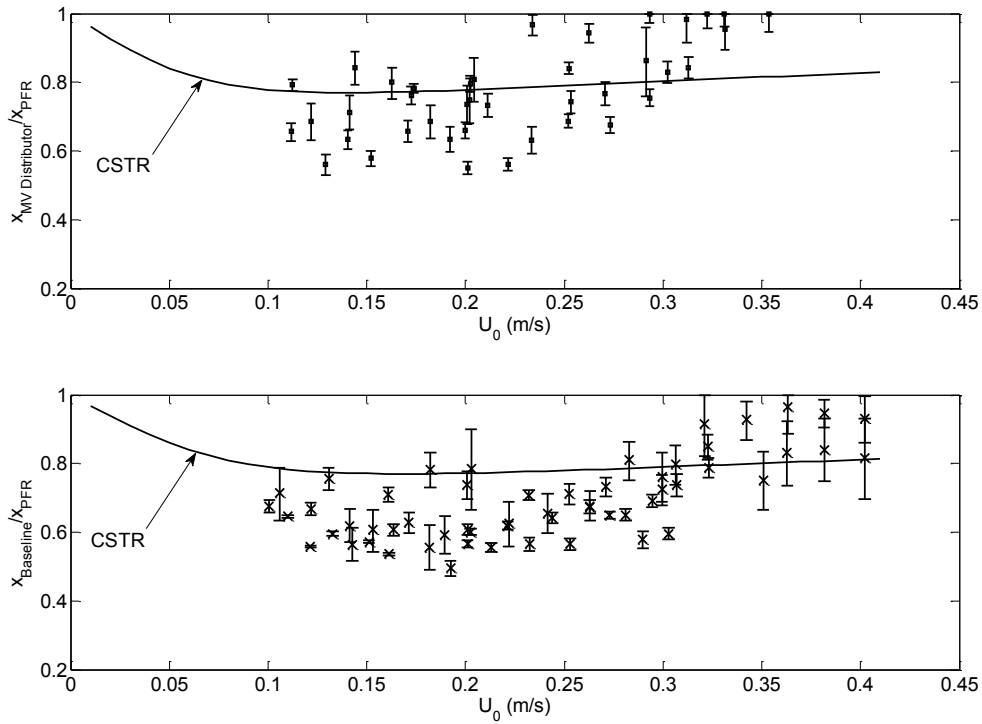


Figure 4-1: The average conversion efficiency for the measured conversions. Error bars show one standard deviation from the average.

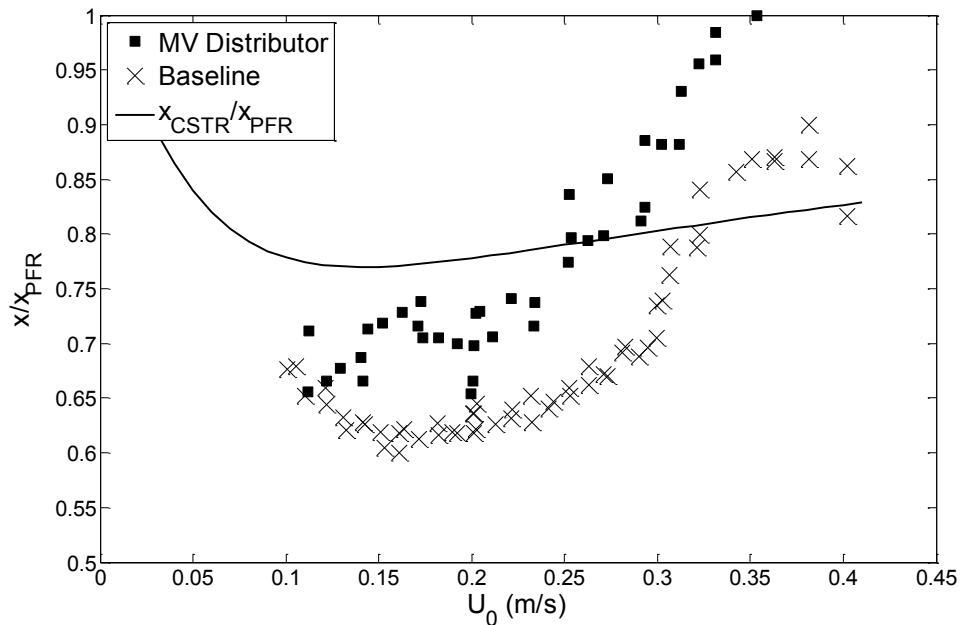


Figure 4-2: The x/x_{PFR} of the MV distributor and the baseline distributor after applying a moving average function over 5 consecutive data points.

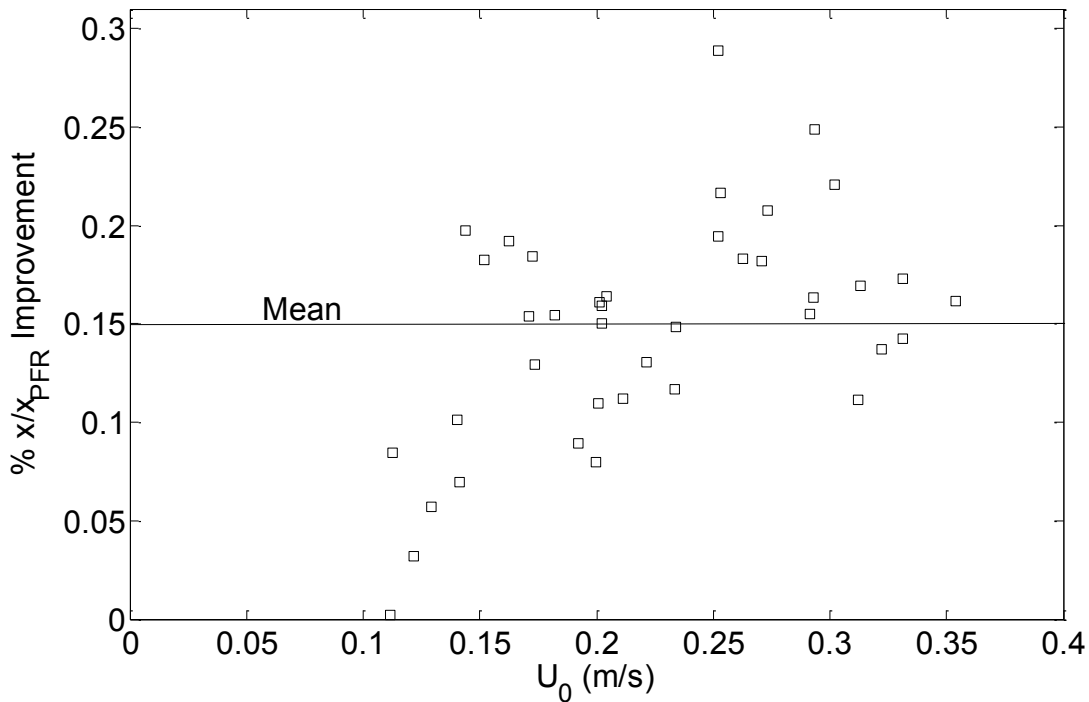


Figure 4-3: The percentage increase in the x/x_{PFR} for the MV distributor. The mean improvement is 14.8%.

4.2 Determining the bubbling to turbulent regime transition boundary

The bubbling to turbulent regime transition boundary is usually determined using the standard deviation of the absolute pressure fluctuations in the FBR (Bi, HT *et al.*, 2000). From Figure 4-4 it can be seen that the maximum of the pressure fluctuations for the baseline case appears to be about 0.30 m/s (U_c).

The MV distributor does not exhibit a turn within the experimental velocity range, however from visual observations (CD attached in Appendix E), using the criteria described in section 2.3.1, it appears that the turbulent transition takes place between 0.20 m/s and 0.30 m/s. From this an $U_c = 0.25$ m/s was chosen as the U_c for the MV distributor.

This shows that the MV distributor causes the FBR to exhibit turbulent behaviour faster than the baseline distributor. This improves the fluidizing behaviour of the FBR, because the turbulent bed is seen to comprise a single phase which negates the existence of interphase mass transfer limitations.

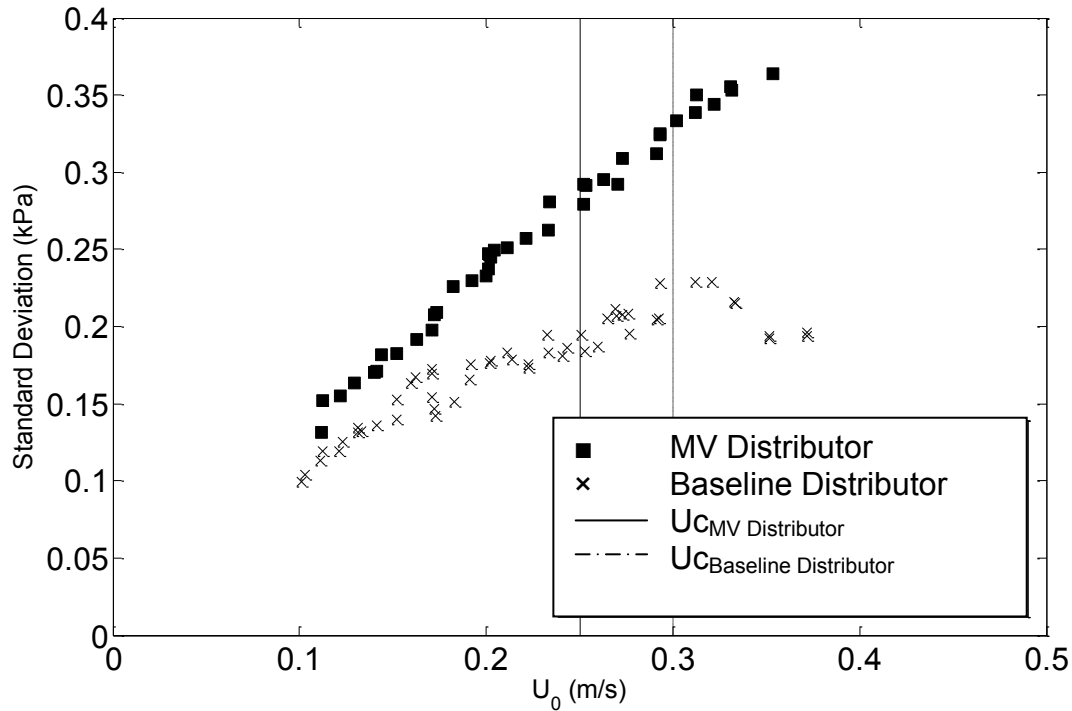


Figure 4-4: The standard deviation of the pressure fluctuations of both the baseline and MV distributor experimental runs.

4.3 Bubbles Sizes

4.3.1 Visual Bubble Size Measurements

The bubble sizes were correlated to the superficial velocity through the column by using a frame by frame analysis of videos taken (Figure 3-7) of the bubbles passing through the bed. This was compared to the incoherent standard deviation ($\sigma_{xy,i}$) of the absolute pressure fluctuations at a height of 0.3 m above the distributor as compared to the pressure fluctuations at the distributor surface. The bubble size measurements are shown in Figure 4-5.

From Figure 4-5 it can be seen that the bubble growth (the slope of each curve) from visual observation is approximately 1.4 times greater when using the MV distributor than in the baseline case.

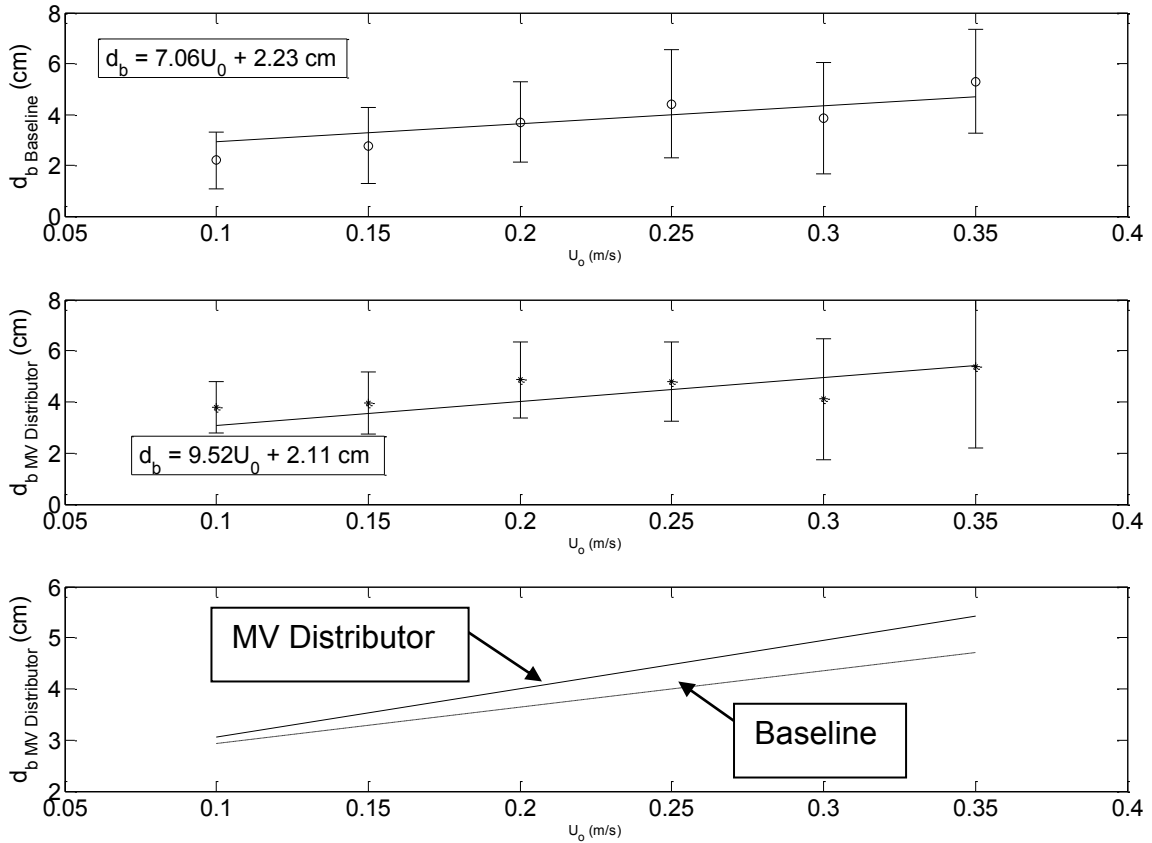


Figure 4-5: The visually measured bubble diameters with the linear correlation of the bubble diameters, shown together in the bottom graph.

4.3.2 Bubble Size Analysis Using Pressure Fluctuations

The standard deviation of the incoherent pressure fluctuations $\sigma_{xy,i}$ in the bed and at the distributor surface are shown in Figure 4-6. This figure shows that the $\sigma_{xy,i}$ in the bed using the MV distributor is roughly 1.4 times the $\sigma_{xy,i}$ in the bed using the baseline distributor. The corresponding correlations are shown in the graphs.

The findings from Figure 4-5 and Figure 4-6 are in agreement and therefore the bubble growth functions shown in Figure 4-5 are used in the modelling of the FBR in the subsequent sections.

Figure 4-6 shows a significant drop in the $\sigma_{xy,i \text{ Baseline}}$ after U_c was crossed in the baseline case. This is significant as it indicates that as the bubbling to turbulent transition boundary was crossed, the gas phase in the FBR has a less pronounced effect on $\sigma_{xy,i \text{ Baseline}}$.

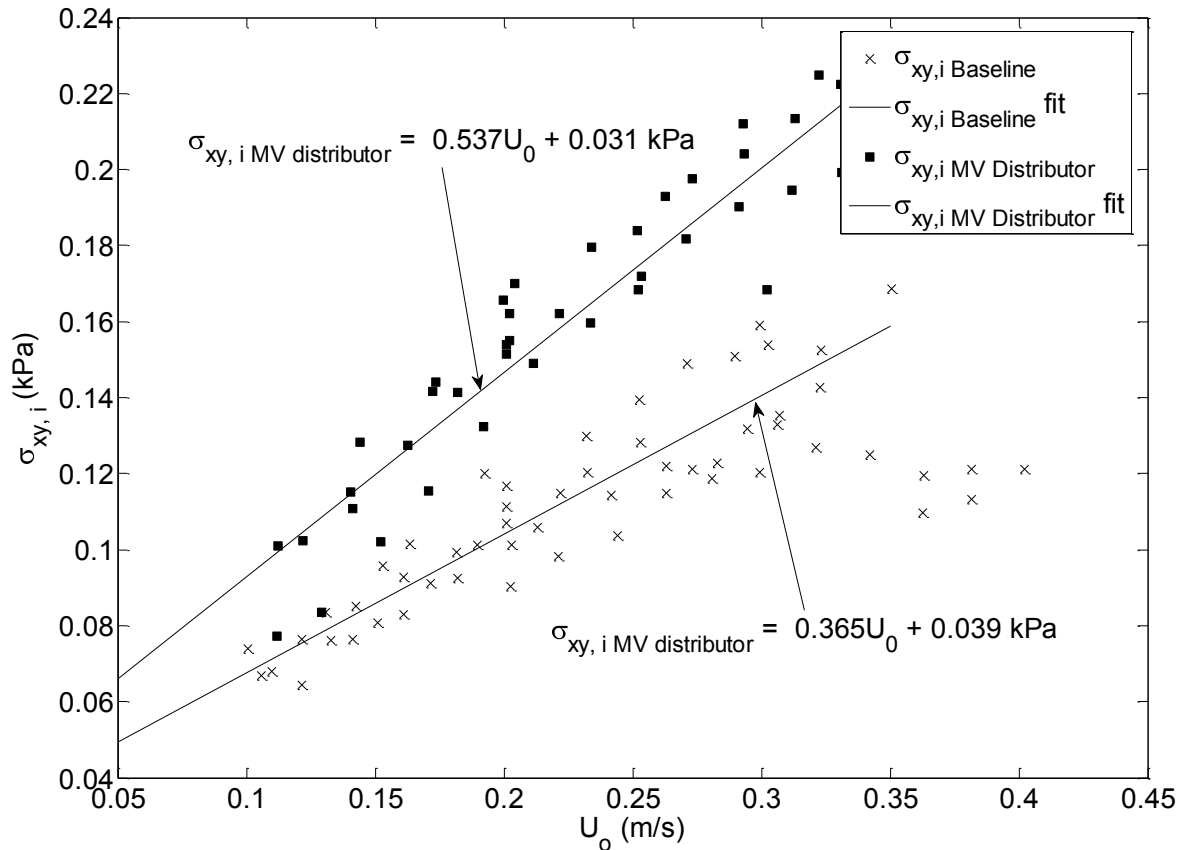


Figure 4-6: The $\sigma_{xy,i}$ of the baseline and the MV distributor used for the analysis of the bubble sizes in the separate experimental studies.

4.4 Model Predictions

4.4.1 Kunii-Levenspiel Model (K-L Model)

The smoothed conversion efficiencies for the experimental studies, the K-L Model and the CSTR conversion efficiencies are shown in Figure 4-7 (top). The corresponding % error plots between the baseline/MV distributor prediction and measured conversion efficiencies are shown in Figure 4-7 (middle and bottom).

From Figure 4-7 it can be seen that the K-L model predicts the measured baseline conversion efficiencies to within $\pm 10\%$ error for U_0 between 0.1 m/s to 0.25 m/s. The K-L model predicts the MV distributor conversion efficiencies to within $\pm 10\%$ error for the velocities between 0.1 m/s and 0.30 m/s. For both these experimental cases the % error increases significantly above the respective velocities which are also the respective distributor U_c values. This is expected as the K-L model does not take into consideration the transition of the FBR from the bubble to turbulent regimes.

Table 4-1 show the model parameters used to fit the experimental conversion efficiencies, the fitted parameters are shown in grey.

Table 4-1: The Variables used for the simulation of the Kunii-Levenspiel model; the fitted parameters are shown in grey

Variable		
Distributor	Perforated Plate	MV Distributor
Column Type	2-D	2-D
\bar{k}_r'''	1.6 s ⁻¹	1.33 s ⁻¹
M_{so}	3	3
Catalyst	FCC	FCC
d_p	87µm	84µm
Bubble size	2.3 cm – 5.1 cm	2.2 cm – 7.7 cm
α	0.3	1
f_b	0.0355δ	0.0355δ
$f_{K_{bc}}$	0.67	0.75
$f_{K_{ce}}$	0.67	0.75
ρ_s	1580 kg/m ³	1580 kg/m ³
ρ_g	1.20 kg/m ³	1.20 kg/m ³

The significance of the fitted parameters α , $f_{K_{bc}}$ and $f_{K_{ce}}$ is discussed in more detail in section 2.5.1.2 (p. 2-13). The fitted values of α indicate that the wake volume seen in the MV distributor is more than three times that of the baseline distributor and is supported by visual observation (Appendix E). The value for f_b is defined as a fitted parameter but a fixed function was derived from the corresponding variable (ϕ_{Lo}) in the Thompson model:

$$f_b = \phi_{Lo}\delta \quad 4-1$$

The literature value for $\phi_{Lo} = 3.55\%$ (Thompson *et al.*, 1999) which therefore fixed the value for f_b .

The final two parameters ($f_{K_{bc}}$ and $f_{K_{ce}}$) are an indication of the mass transfer in the FBR for the respective distributors. The improvement in mass transfer seems to be in the order of 12% which compares well with the improvement seen in Figure 4-3.

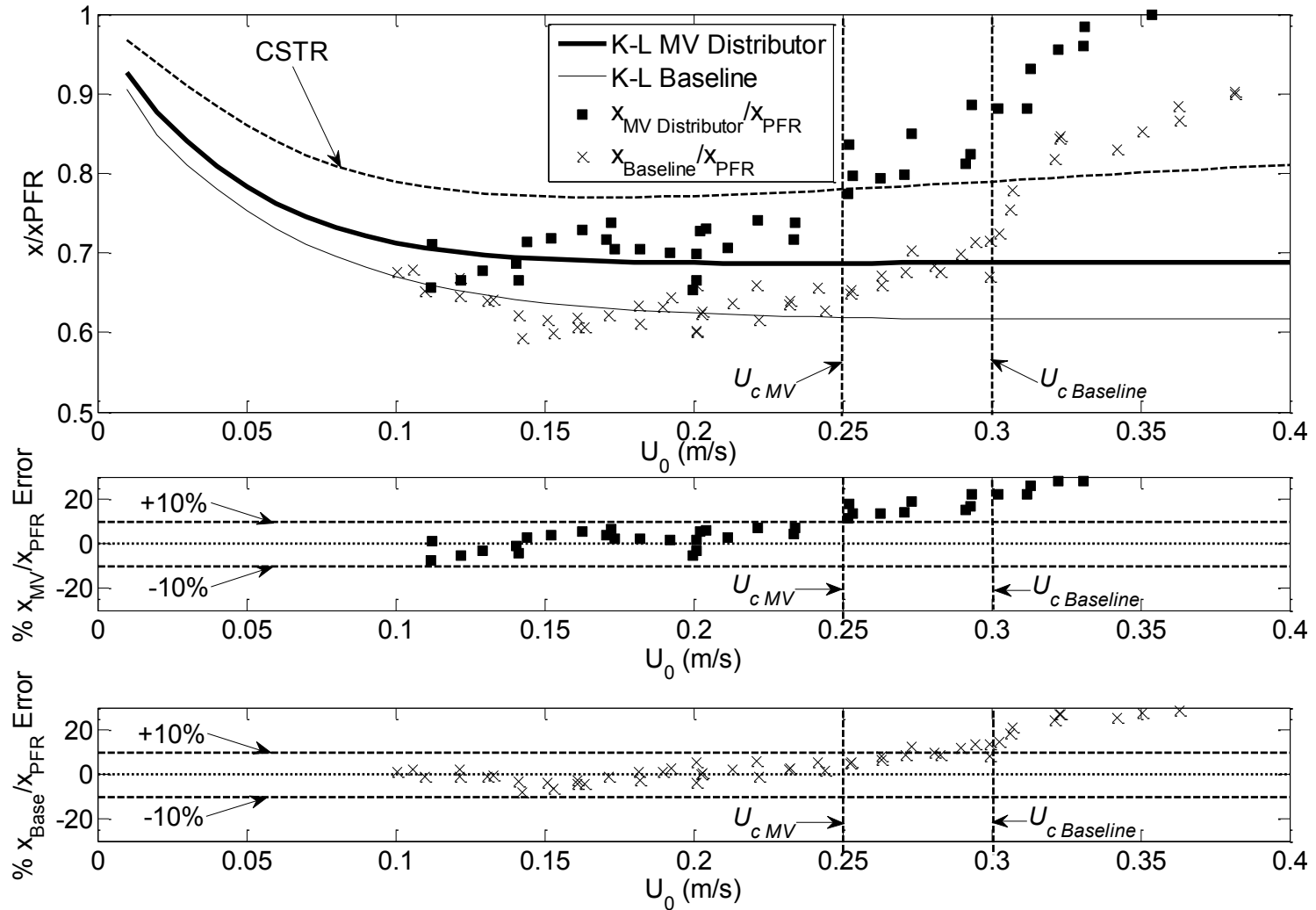


Figure 4-7: **Top:** The K-L model predictions for the measured conversion efficiencies for both the baseline and the MV distributor. **Middle and Bottom:** The % Error plots for the baseline and MV distributor

4.4.2 Thompson Model

Figure 4-8 shows the smoothed conversion efficiencies of the baseline and the MV distributor, together with the respective % error plots of each. From the results it can be seen that the model predicts the measured conversion efficiencies to within 10% error. Table 4-2 shows the comparative variables fitted for the different studies, with the fitted parameters shown in bold. The column on the far right (light grey) show values fitted for experimental results measured in a 3-D bed (Thompson *et al.*, 1999).

Table 4-2: The Variables used for the simulation of the Thompson model; the fitted parameters are shown in dark grey

Variable	Current Study		Thompson <i>et al.</i> (1999)
Distributor	Perforated Plate	MV Distributor	Perforated Plate
Column Type	2-D	2-D	3-D
$\overline{k_r''''}$	1.6 s ⁻¹	1.33 s ⁻¹	2.41 s ⁻¹
M_{so}	3.6	3.6	5
Catalyst	FCC	FCC	FCC
d_p	87µm	84µm	60 µm
Bubble size	2.3 cm – 5.1 cm	2.2 cm – 7.7 cm	8 cm
f_c	0.2	0.2	0.2
f_{k_q}	0.47	0.75	2.023
f_{Pe}	0.45	13	0.247
Φ_{Lo}	3.55%	3.55%	3.55%
μ_g	2.0 x 10 ⁻⁵ Pa.s	2.0 x 10 ⁻⁵ Pa.s	2.0 x 10 ⁻⁵ Pa.s
ρ_s	1580 kg/m ³	1580 kg/m ³	1580 kg/m ³
ρ_g	1.20 kg/m ³	1.20 kg/m ³	1.20 kg/m ³

The significance of the fitted variables is discussed in section 2.5.3.3 (p. 2-22). The fitted values for f_{k_q} show that an increase in mass transfer is apparent, the k_q for the MV distributor is approximately 60% higher than the baseline distributor.

In addition Table 4-2 show that the f_{Pe} for the MV distributor is significantly larger (53 times larger) than the fitted value in the 3-D bed. Comparatively the fitted value in the bed with the baseline distributor the f_{Pe} only differs by a factor of two. This shows

that the FBR with the MV distributor acts significantly more like a PFR in the turbulent regime than either the bed with the baseline distributor or the 3-D bed; the axial dispersion in the bed is much lower than expected from the Pe correlation (equation 2-44). This observation is supported by the nearly perfect x/x_{PFR} measured in with the MV distributor as $U_0 \rightarrow U_\infty$ (Figure 4-8).

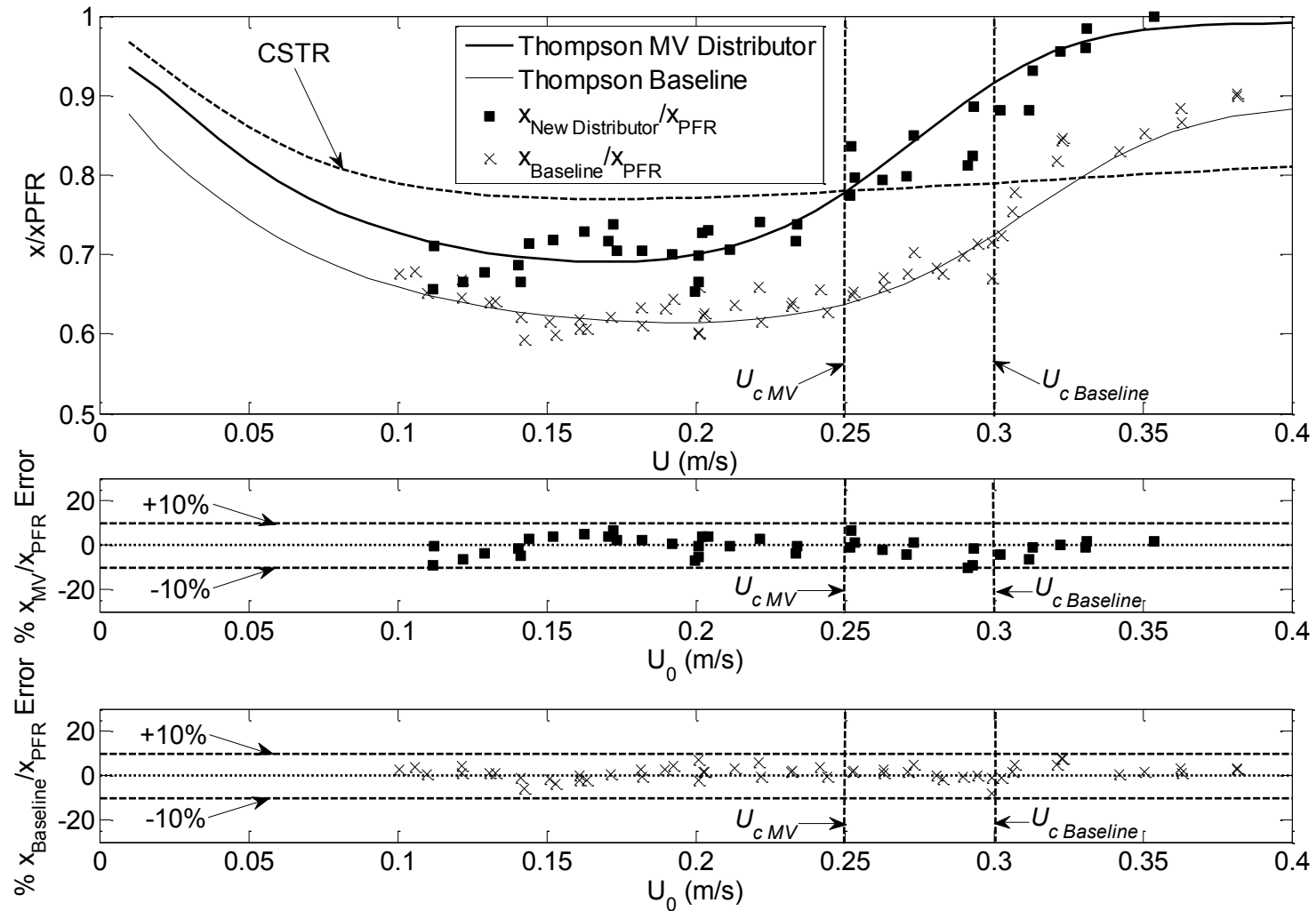


Figure 4-8: **Top:** The Thompson model predictions for the measured conversion efficiencies for both the baseline and the MV distributor. Also shown is the CSTR model for the respective distributor cases. **Middle and Bottom:** The % Error plots for the baseline and MV distributor.

5 Conclusions

From the comparative study of the influence of a MV distributor and a perforated plate distributor on the performance of a 2-D FBR the following conclusions were drawn:

- The MV distributor caused a significant improvement in the conversion efficiencies at all velocities tested, the improvement ranged between 0% and 20% improvement, with an average improvement of 14.7%. At $U_0 \geq 0.2 \text{ m/s}$ the improvement distributed evenly about the mean improvement, with a minimum improvement of 10%.
- The bubble size growth for the MV distributor was estimated to be 1.4 times greater than that of the baseline.
- The fitted parameter for the two models showed that
 - the mass transfer for the MV distributor is significantly larger than that of the baseline.
 - The MV distributor decreased the axial dispersion in the FBR at high velocities which improved the reactor performance to close to that of an ideal PFR.
- The U_c for the MV distributor was less than that for the baseline distributor, which showed that the onset of turbulent behaviour in the FBR was faster for the MV distributor than for the baseline distributor:
 - $U_{c \text{ Baseline}} = 0.30 \text{ m/s}$
 - $U_{c \text{ MV distributor}} = 0.25 \text{ m/s}$

From these conclusions it can be seen that the MV distributor improves the reactor performance for the bubbling and turbulent regime by increasing the interphase mass transfer in the bubbling bed, decreasing the axial dispersion in the turbulent bed and inducing a faster transition from bubbling to turbulent behaviour in the FBR.

6 References

Abba, IA, Grace, JR, Bi, HT and Thompson, ML (2003) "Spanning the flow regimes: generic fluidized-bed reactor model" *AIChE J.*, 49(7), 1838 - 1848.

Bi, HT, Ellis, N and Grace, JR (2000) "A state-of-the-art review of gas-solid turbulent fluidization" *Chem. Eng. Sci.*, 55(21), 4789 - 4825.

Bi, HT, Grace, JR and Lim, KS (1995) "Transition from bubbling to turbulent fluidization" *Ind. Eng. Chem. Res.*, 34(11), 4003 – 4008.

Brink, HG (2011) "Perforated plate and Multi vortex distributor in a 2D fluidized bed reactor compared", <http://www.youtube.com/watch?v=qWH4MHR4IQo> [2011, June 21].

Christensen, D, Nijenhuis, J, Van Ommen, JR and Coppens, MO (2008) "Influence of distributed secondary gas injection on the performance of a bubbling fluidized-bed reactor" *Ind. Eng. Chem. Res.*, 47(10), 3601 - 3618.

Christensen, D, Vervloet, D, Nijenhuis, J, Van Wachem, BGM and Van Ommen, J R (2008) "Insights in distributed secondary gas injection in a bubbling fluidized bed via discrete particle simulations" *Powder Technol.*, 183(3), 454 - 466.

Chyang, CS, Lieu, K and Hong, SS (2008) "The effect of distributor design on gas dispersion in a bubbling fluidized bed" *J. Chin. Inst. Chem. Eng.*, 39(6), 685 – 692.

Chyang, CS and Lin, YC (2002) "A study in the swirling fluidizing pattern" *J. Chem. Eng. Jpn.*, 35(6), 503 - 512.

Depypere, F, Pieters, JG and Dewettinck, K (2004) "CFD analysis of air distribution in fluidised bed equipment" *Powder Technol.*, 145(3), 176 - 189.

Fan, C, Zhang, Y, Bi, X, Song, W, Lin, W and Luo, L (2008) "Evaluation of downer reactor performance by catalytic ozone decomposition" *Chem. Eng. J.*, 140(1-3), 539 – 554.

Fogler, HS (2006) *Elements of Chemical Reaction Engineering* (4th Ed.), Pearson Education Inc., NJ, USA.

Garncarek, Z, Przybylski, L, Botterill, JSM and Broadbent, CJ (1997) "A quantitative assessment of the effect of distributor type on particle circulation" *Powder Technol.*, 91(3), 209 – 216.

Geldart, D and Cranfield, RR (1972) "The gas fluidisation of large particles" *Chem. Eng. J.*, 3, 211.

Grace, JR (1984) "Generalized models for isothermal fluidized bed reactors" in *Recent Advances in the Engineering Analysis of Chemically Reacting Systems*, L.K. Doraiswamy (Ed.), Wiley Eastern, New Delhi, India.

Hulme, I and Kantzas, A (2004) "Determination of bubble diameter and axial velocity for a polyethylene fluidized bed using X-ray fluoroscopy" *Powder Technol.*, 147(1-3), 20 - 33.

Kehoe, PWK and Davidson, JF (1970) "Continuously slugging fluidized beds" in *Chemeca '70, Institution of Chemical Engineers Symposium Series*, 97 – 116, Butterworths, Australia.

Kleijn van Willigen, F, Christensen, D, Van Ommen, JR and Coppens, MO (2005) "Imposing dynamic structures on fluidised beds" *Catal. Today*, 105(34), 560 – 568.

Köksal, M and Vural, H (1998) "Bubble size control in a two-dimensional fluidized bed using a moving double plate distributor" *Powder Technol.*, 95(3), 205 - 213.

Kunii, D and Levenspiel, O (1991) *Fluidization Engineering* (2nd ed.). Butterworth-Heinemann, USA.

Leung, LS (1972) "Design of gas distributors and prediction of bubble size in large gas-solids fluidized beds" *Powder Technol.*, 6(4), 189 - 193.

Levenspiel, O (1999) *Chemical Reaction Engineering* (3rd Ed.), John Wiley & Sons, Inc., New York.

Lombardi, G, Pagliuso, JD and Goldstein, L (1997) "Performance of a tuyère gas distributor" *Powder Technol.*, 94(1), 5 - 14.

Ouyang, F and Levenspiel, O (1986) "Spiral distributor for fluidized beds" *Industrial Ind. Eng. Chem. Proc. D. D.*, 25(2), 504–507.

Ouyang, S, Lin, J and Potter, OE (1993) "Ozone decomposition in a 0.254m diameter circulating fluidized bed reactor" *Powder Technol.*, 74(1), 73 - 78.

Pagliolico, S, Tiprigan, M, Rovero, G and Gianetto, A (1992) "Pseudo-homogeneous approach to CFB reactor design" *Chem. Eng. Sci.*, 47(9-11), 2269–2274.

Rowe, PN, Santoro, L and Yates, JG (1978) "The division of gas between bubble and interstitial phases in fluidised beds of fine powders" *Chem. Eng. Sci.*, 33(1), 133 - 140.

Saayman, J. (2009) *Bubbling to Turbulent Regime Transition in a 2D Catalytic Fluidized Bed Reactor*, Masters Thesis, University of Pretoria , Pretoria, South Africa.

Sathiyamoorthy, DS and Rao, CS (1978) "Gas distributor in fluidized beds" *Powder Technol.*, 20, 47 - 52.

Schoenfelder, H, Kruse, M and Werther, J (1996) "Two-dimensional model for circulating fluidized-bed reactors" *AIChE J.*, 42(7), 1875 – 1888.

Shen, L, Johnsson, F and Leckner, B (2004) "Digital image analysis of hydrodynamics two-dimensional bubbling fluidized beds" *Chem. Eng. Sci.*, 59(13), 2607 – 2617.

Sobrinho, C, Acosta-Iborra, A, Santana, D and De Vega, M (2009) "Bubble characteristics in a bubbling fluidized bed with a rotating distributor" *Int. J. Multiphase Flow*, 35(10), 970 - 976.

Sreenivasan, B and Raghavan, VR (2002) "Hydrodynamics of a swirling fluidised bed" *Chem. Eng. Process.*, 41(2), 99 – 106.

Sun, G and Grace, J (1990) "The effect of particle size distribution on the performance of a catalytic fluidized bed reactor" *Chem. Eng. Sci.*, 45(8), 2187 - 2194.

Thompson, M.L, Bi, HT and Grace, JR (1999) "A generalized bubbling/turbulent fluidized-bed reactor model" *Chem. Eng. Sci.*, 54, 2175 - 2185.

Upadhyay, SN, Saxena, SC and Ravetto, FT (1981) "Performance characteristics of multijet tuyere distributor plates" *Powder Technol.*, 30(2), 155 – 159.

Van der Schaaf, J, Schouten, JC, Johnsson, F and Van den Bleek, CM (2002) “Non-intrusive determination of bubble and slug length scales in fluidized beds by decomposition of the power spectral density of pressure time series” *Int. J. Multiphase Flow*, 28(5), 865 – 880.

Van Ommen, JR, Nijenhuis, J and Coppens, MO (2009) “Reshaping the Structure of Fluidized Beds” *Chem. Eng. Prog.*, July, 49-57.

Werther, J (1978) “Effect of gas distributor on the hydrodynamics of gas fluidized beds” *Ger. Chem. Eng.*, 1, 166.

Wormsbecker, M, Pugsley, TS and Tanfara, H (2007) “The influence of Distributor Design on Fluidized Bed Dryer Hydrodynamics”, paper presented at *The 12th International Conference on Fluidization-New Horizons in Fluidization Engineering*, 13 - 17 May, 2007, Vancouver, Canada.

Yan, A, Huang, W and Zhu, J (2008) “The influence of distributor structure on the solid distribution and flow development in circulating fluidized beds” *Can. J. Chem. Eng.*, 86, 1023 - 1031.

Yang, WC (2003a) “Preface” in *Handbook of Fluidization and Fluid-Particle Systems*, iii-iv, Yang, W. C. (Ed.), Marcel Dekker, Inc., New York.

Yang, WC (2003b) “Bubbling Fluidized Beds” in *Handbook of Fluidization and Fluid-Particle Systems*, 53-111, Yang, W. C. (Ed.), Marcel Dekker, Inc., New York.

Zimmermann, S and Taghipour, F (2005) “CFD modeling of the hydrodynamics and reaction kinetics of FCC fluidized-bed reactors” *Ind. Eng. Chem. Res.*, 44(26), 9818 – 9827.

Appendix A List of Investigations on the Bubble-Emulsion Separation in FBRs

Table A-1: Investigations into the bubble-emulsion separation limitations in FBRs

Author	Investigated method to improve interphase limitations in a FBR
Leung (1972)	Reducing bubble size by designing distributor with correct pitch and hole sizes
Rowe <i>et al.</i> (1978)	Increasing interstitial flow in emulsion by decreasing the particle size distribution; addition of fines
Werther, (1978)	Distribution of bubbles using different types of distributors
Sathiyamoorthy & Rao (1978)	Effect of bed height and bed materials on orifice operation and therefore FBR operation
Upadhyay <i>et al.</i> (1981)	Performance of multijet tuyère type distributor on FBR performance
Ouyang, F & Levenspiel, (1986); Sreenivasan & Raghavan (2002)	Spiral distributor performance and hydrodynamic characteristic
Garncarek <i>et al.</i> (1997)	Comparison of hydrodynamic mixing of a porous and perforated plate distributor
Lombardi <i>et al.</i> (1997)	Flow pattern and discharge coefficient of a tuyère distributor
Chyang & Lin, YC (2002)	Comparison of hydrodynamics of a swirling distributor (radial and axial momentum) and a perforated plate distributor (axial momentum)
Depypere <i>et al.</i> (2004)	Simulation of the performance of different distributor types using CFD analysis
Kleijn van Willigen <i>et al.</i> (2005)	Electric field enhanced fluidisation and distributed secondary gas injection by a fractal injector
Wormsbecker <i>et al.</i> (2007)	Perforated plate, punched plate and Dutch weave distributor effect on FBR performance
Yan <i>et al.</i> (2008)	Comparison of solid distribution in a FBR with a multi orifice distributor and a multi-tube distributor
Christensen <i>et al.</i> (2008)	Effect of secondary injection of fluidizing gas on FBR performance
Chyang <i>et al.</i> (2008)	Tuyère and horizontal nozzle distributor performance in a FBR
Van Ommen <i>et al.</i> (2009)	Decoupling of mass transfer limitations using diverse methods

Appendix B Distributor Types and Respective Advantages and Disadvantages (Kunii & Levenspiel, 1991:95)

Table B-1: Commonly Used Distributors with Advantages/ Disadvantages

Distributor Types	Advantages	Disadvantages
Perforated Plates	<ul style="list-style-type: none"> • Simple fabrication • Most common • Inexpensive • Easy to modify • Easy up- or downscaling • Easy cleaning • Concave/convex/double dished • Ports easily shrouded 	<ul style="list-style-type: none"> • Weepage • Buckling/thermal distortion • Peripheral seal • Requires support if long span • High pressure drop
Bubble Caps and Nozzles	<ul style="list-style-type: none"> • Weepage reduced/avoided • Good turndown • Caps introduced to stiffen design • Support internals 	<ul style="list-style-type: none"> • Expensive • Stagnant regions • Subject to immediate bubble merger • Difficult to clean • Difficult to modify • Not for sticky solids • Peripheral seal • Ports not easily shrouded
Spargers	<ul style="list-style-type: none"> • Minimize weeping • Good turndown • Low pressure drop • Support internals • Thermal expansion without damage • Easily shrouded ports • Suited to multi level injection • Solids above and below the grid 	<ul style="list-style-type: none"> • Defluidized solids below the grid • Less forgiving mechanical design

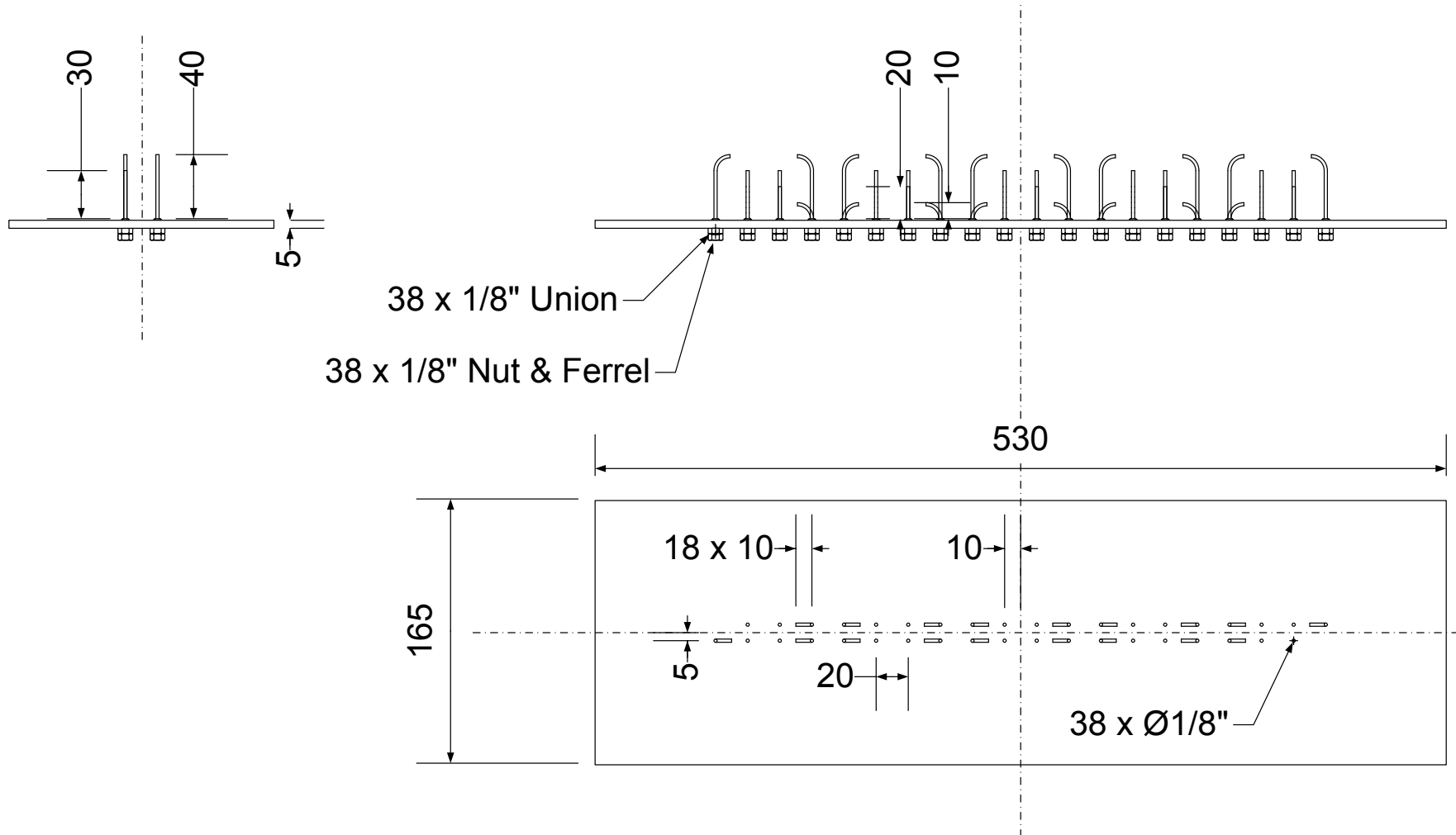
Conical Grids

- Promotes solid mixing
- Prevents stagnant solids buildup
- Minimizes solids segregation
- Easy discharge of solids
- Difficult to construct
- Careful design for good gas distribution
- High pressure drop for good distribution

Pierced Sheet Grids

- Good solids mix
- Prevents stagnant solids buildup.
- Facilitates discharge of most of the solids
- Holes angled to prevent weeping
- Difficult to construct
- Small hole sizes
- Requires reinforcing to support the bed

Appendix C Mechanical Drawing of MV Distributor Design



Appendix D Particle Size Distributions for Respective Distributor Experiments

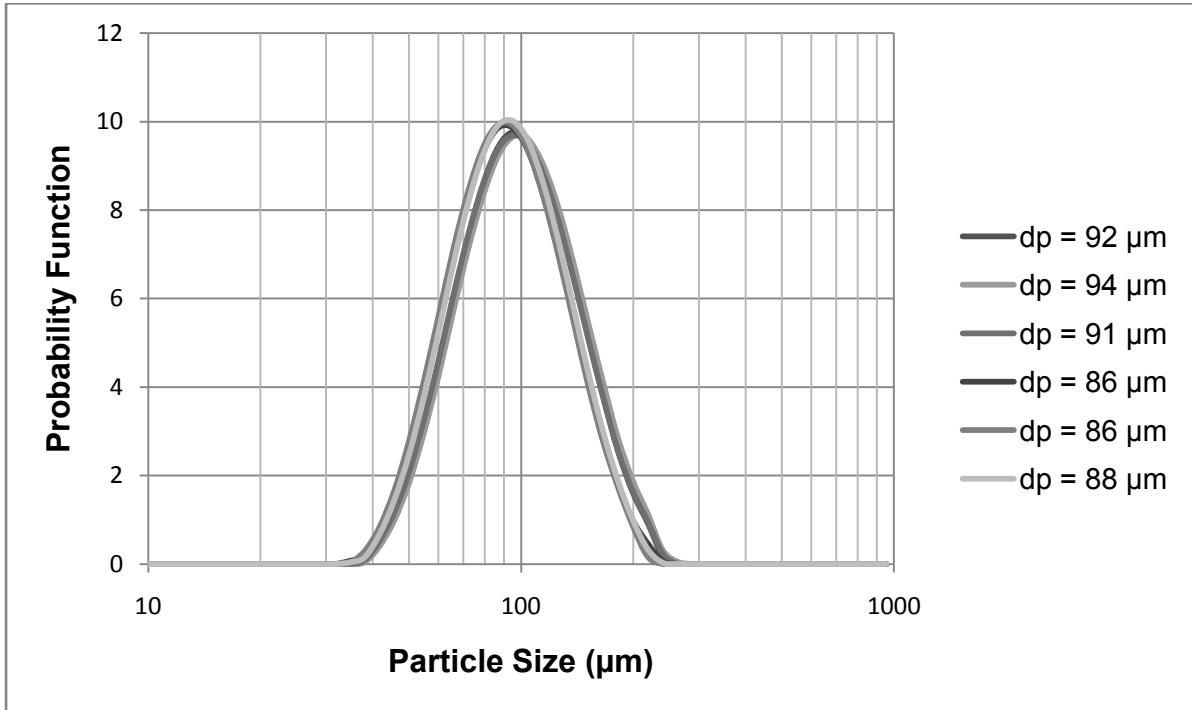


Figure D-1: The particle size distributions for the baseline distributor experiments. The legend is shown chronologically. The average $d_p = 87 \mu\text{m}$.

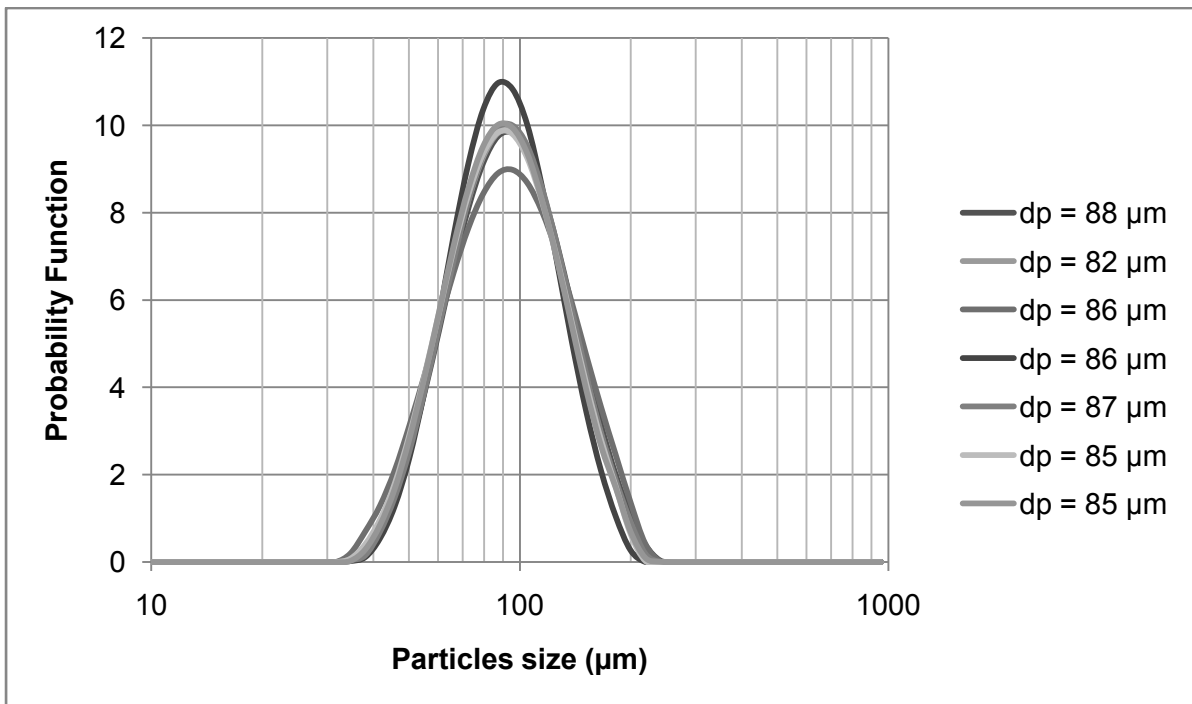


Figure D-2: The particle size distributions for the MV distributor experiments. The legend is shown chronologically. The average $d_p = 84 \mu\text{m}$.

Appendix E Video of Comparative Behaviour seen in Respective Distributor Experiments

The video is available for viewing at the following URL as an upload from the author (Brink, 2011):

<http://www.youtube.com/watch?v=qWH4MHR4IQo>